Lawrence Berkeley National Laboratory
Recent Work

Title
POLARIZATION AND DIFFERENTIAL CROSS SECTIONS IN PROTON-PROTON AND PROTON-NUCLEUS SCATTERINGS AT 730 MeV

Permalink

Author
McManigal, Paul G.

Publication Date
1963-03-15

University of California

Ernest O. Lawrence Radiation Laboratory

Berkeley, California

DISCLAIMER

UNIVERSITY OF CALIFORNIA

Lawrence Radiation Laboratory
Berkeley, California

Contract No. W-7405-eng-48

POLARIZATION AND DIFFERENTIAL CROSS SECTIONS
IN PROTON-PROTON AND PROTON-NUCLEUS SCATTERINGS
AT 730 MeV

Paul G. Mc Manigal

(Thesis)

March 15, 1963

POLARIZATION AND DIFFERENTIAL CROSS SECTIONS
IN PROTON-PROTON AND PROTON-NUCLEUS SCATTERINGS
AT 730 MeV

Contents

POLARIZATION AND DIFFERENTIAL CROSS SECTIONS
IN PROTON-PROTON AND PROTON-NUCLEUS SCATTERINGS
AT 730 MeV

Paul G. Mc Manigal

(Thesis)

Lawrence Radiation Laboratory
University of California
Berkeley, California

March 15, 1963

ABSTRACT

The polarization and angular distribution of protons scattered from protons, helium, beryllium, carbon, aluminum, calcium, iron and tantalum were measured as functions of angle at 730 MeV. A variation of the usual double-elastic-scattering method was used, in that the sense of the first scattering angle was reversed in finding asymmetries rather than the second angle. Elasticity of scattering was favored by a 102-deg magnetic spectrometer which clearly separated particles losing more than 15 MeV in scattering. The polarization in proton-proton scattering reaches a maximum of more than 60%, while polarization obtained from scattering from other nuclei remains lower. The polarized angular distribution indicates that the $^3F_4$ state or higher waves of odd parity must play a significant role in proton-proton scattering. The proton-nucleus scattering was fitted by an optical model.

I. INTRODUCTION

The study of nucleons scattering at high energies by nucleons and nuclei has provided a considerable body of information about the radial and spin dependence and magnitude of the nuclear interaction. The first measurements were of the total cross sections. In the Born approximation they yield information on a volume integral over the strength of the interaction. Ambiguities exist as to whether there is a strong interaction over a short range or a weak interaction over longer distances. A knowledge of the differential cross section removes these ambiguities by revealing the interaction's radial dependence. From nucleon-nucleon differential cross sections we learn which angular-momentum states are interacting. Since high-energy nucleons have a short de Broglie wave length and sufficient energy to probe the nucleus, we learn from nucleon-nucleus differential scatterings the radial distributions of nuclear matter. It takes a study of polarization phenomena, however, to determine the role of the nucleon's spin in the interaction. Only if the strength of the interaction depends on the spin states can there be any polarization effects. By contrasting the nucleon-nucleon scattering with nucleon-nucleus scattering we can learn the validity of the direct-interaction model. In that model, two-body processes determine the nucleon-nucleus scatterings rather than the nucleon interacting with the whole or subunits of the nucleus.

For a detailed review of previous work the reader is referred to four encompassing review articles; the work of MacGregor et al. on nucleon-nucleon scattering,[1] Feshbach's justification of the optical model,[2] and Wolfenstein's[3] and Squire's[4] reviews of polarization effects. A few of the early measurements are mentioned here. Richardson et al. in 1952 observed the differential cross section of protons scattering elastically from various nuclei.[5] The data were fit by Gatha and Riddell[6] by using an optical model with complex central nuclear potential of the form suggested by Fernbach et al.[7] Seeking another criterion for differentiating between different nuclear-potential

models, Oxley et al. succeeded in obtaining the first high-polarization measurements with a high-energy proton beam.[8] Chamberlain et al. pursued this work by measuring the differential cross section and polarization at 310 MeV.[9] Many other groups have made similar measurements in the neighborhood of a few hundred MeV. Measurements by Mescheriakov et al. at 635 MeV are closest in energy to the work reported herein.[10-12]

To explain polarization phenomena in nucleon-nucleus scattering, Fermi postulated a potential V_s which depends on the gradient of the central potential V_c times the product of the orbital angular momentum $\vec{l}$ and the nuclear spin $\vec{\sigma}$:[13]

$$V_s \propto \frac{1}{r} \frac{\partial V_c}{\partial r} \vec{l} \cdot \vec{\sigma} .$$

By the use of the gradient of the central potential, the spin-orbit effects are restricted to the edge of the nucleus. When this non-central potential is added to the central potential, the shapes and the magnitudes of the polarization as functions of angle can be fitted.

In this experiment we measured the differential cross section and the polarization of protons incident at 730-MeV lab energy scattering from eight different elements including hydrogen. Great care has been taken to look at the elastic scatterings. Freedom from systematic error allowing high accuracy in the polarization results is due to the new laboratory technique of varying the sense of the first scattering angle rather than the second to obtain asymmetries.

II. THEORY

A. General Formulation

The intensity and polarization of a beam of spin-1/2 particles can be characterized by the expectation value of four 2-by-2 orthogonal matrices. The usual choice for these matrices is the identity matrix and the three Pauli spin matrices. We can define an intensity by[14]

$$I = (\psi^\dagger, \psi),$$

and the intensity times the polarization by

$$I\vec{P} = (\psi^\dagger, \vec{\sigma}\psi),$$

where ψ is the spin wave function for the beam of particles, and the cross denotes the Hermitian conjugate.

The wave function at a large distance from the region of interaction of a beam of spin-1/2 particles with a target may be written in the form

$$\psi(r) \sim e^{ikz}\chi_i + \psi_f(\theta, \phi)\frac{e^{ikr}}{r}.$$

Here all coordinates are in the center of mass, k is the momentum, the incoming beam is along the z axis, χ_i is the initial spin function, and r is the distance from the interaction. The scattering amplitude, $\psi_f(\theta, \phi)$, is dependent on the conventional spherical polar and azimuthal angles and may be generally written

$$\psi_f(\theta, \phi) = M(\theta, \phi)\chi_i.$$

The general form of the scattering matrix that describes the interaction between a spin-1/2 and a spin-zero particle has been shown to be[15]

$$M(\theta, \phi) = A(\theta) + \vec{\sigma} \cdot \vec{n} B(\theta).$$

Here A and B are complex functions of only the polar angle θ, $\vec{\sigma}$ is the spin, and $\vec{n}$ is a vector perpendicular to the plane of scattering defined by the relation

$$\vec{n} = \frac{\vec{k} \times \vec{k}'}{|\vec{k} \times \vec{k}'|} ,$$

where $\vec{k}$ and $\vec{k}'$ are the incident and final momenta of the incident particle in the c. m. system.

For a beam of polarization P_0 scattering from a spin-zero target, the intensity--that is, the differential cross section--is then

$$I(\theta, \phi) = (\psi_f^\dagger, \psi_f) = |A(\theta)|^2 + |B(\theta)|^2 + 2 \operatorname{Re} A^*(\theta) B(\theta) \vec{P}_0 \cdot \vec{n} . \tag{1}$$

The product of the intensity times the polarization is

$$I(\theta), \phi) \vec{P}(\theta, \phi) = (\psi_f^\dagger, \vec{\sigma} \psi_f) = (|A(\theta)|^2 - |B(\theta)|^2) \vec{P}_0 + 2|B(\theta)|^2 (\vec{P}_0 \cdot \vec{n}) \vec{n}$$

$$+ 2 \operatorname{Im} A^*(\theta) B(\theta) \vec{P}_0 \times \vec{n} + 2 \operatorname{Re} A^*(\theta) B(\theta) \vec{n} .$$

For an unpolarized incident beam we have, $\vec{P}_0 = 0$, and the above formulae reduce to

$$I_0(\theta) = |A(\theta)|^2 + |B(\theta)|^2 \tag{2}$$

and

$$I_0(\theta) \vec{P}(\theta) = 2 \operatorname{Re} A(\theta)^* B(\theta) \vec{n}. \tag{3}$$

Using the above formula for P, we can now rewrite Eq. (1) in the form

$$I(\theta, \phi) = I_0(\theta) \left[1 + \vec{P}_0 \cdot \vec{P}(\theta) \right] .$$

We can define the product of the polarizations as the asymmetry, ϵ, and write

$$I(\theta, \phi) = I_0(\theta) \left[1 + \epsilon(\theta) \cos \phi \right] , \tag{4}$$

where ϕ is the angle between $\vec{P}_0$ and $\vec{P}$. We may also choose to think of the second scattering as an "analyzer" and the asymmetry the product of the polarization of the beam times the analyzing power of the

target. It is well to remember that the equivalence of the analyzing power of a target and its polarizing power is a consequence of time reversal, which we have implied by our choice of the scattering matrix. For inelastic scatterings this equivalence is not generally true.

For two spin-1/2 particles, a similar but more complex situation prevails. The scattering matrix M has been derived by Wolfenstein and Ashkin.[16] For the special case of proton-proton scattering, Wolfenstein[15] has shown that the scattering matrix may be written as

$$M(\theta, \phi) = B(\theta)S + C(\theta)(\vec{\sigma} + \vec{\sigma}_t) \cdot \vec{n} + \frac{1}{2} G(\theta)(\vec{\sigma} \cdot \vec{K}\vec{\sigma}_t \cdot \vec{K} + \vec{\sigma} \cdot \vec{P}\vec{\sigma}_t \cdot \vec{P})T$$

$$+ \frac{1}{2} H(\theta)(\vec{\sigma} \cdot \vec{K}\vec{\sigma}_t \cdot \vec{K} - \vec{\sigma} \cdot \vec{P}\vec{\sigma}_t \cdot \vec{P})T + N(\theta)(\vec{\sigma} \cdot \vec{n}\vec{\sigma}_t \cdot \vec{n})T. \tag{5}$$

Here B, C, G, H, and N are complex scalar functions of θ, the singlet and triplet projection operators are denoted S and T, respectively, $\vec{\sigma}$ and $\vec{\sigma}_t$ are the spins of the incident and target protons, and $\vec{K}$ and $\vec{P}$ are unit vectors in the directions $\vec{k}' - \vec{k}$ and $\vec{k}' + \vec{k}$, respectively. The differential cross section for an unpolarized beam analogous to Eq. (2) is

$$I_0(\theta) = \frac{1}{4} |B(\theta)|^2 + 2|C(\theta)|^2 + \frac{1}{4} |G(\theta) - N(\theta)|^2 + \frac{1}{2} |N(\theta)|^2 + \frac{1}{2} |H(\theta)|^2,$$

and the intensity times the polarization analogous to Eq (3) is

$$I_0(\theta) \vec{P}(\theta) = 2 \, \mathrm{Re} \, C^*(\theta) N(\theta) \vec{n}.$$

For two spin-1/2 particles scattering elastically, we may also make the association of the asymmetry with the product of the polarization of the beam and the polarizing power of the target, and further equate polarizing power with analyzing power.

In general one can expand the scalar functions of angle in terms of a power series of Legendre polynomials. Theoretically this is seen possible by quantizing the incident wave into angular-momentum

states. The coefficients in these expansions contain phase shifts of the various waves. Solutions for these phase shifts have been found at energies up to 400 MeV for nucleon-nucleon scattering.[1,17] Single-, double-, and triple-scattering measurements are necessary to determine these phase shifts. With the strength of the inelastic production at 730 MeV, the phase shifts are complex, and many more measurements in addition to the ones reported here must be made before unique values for phase shifts through this energy become known. However, by plotting the data obtained vs $\cos^2\theta$, we can make rudimentary statements as to which waves are participating in the interaction.

Because of the number of angular-momentum waves interacting in the proton-nucleus scatterings, phase-shift analysis is only attempted at the very low energies. Two alternate approaches employed are the optical model and the direct-interaction model.[18] In the direct-interaction model, the scattering of a particle by a nucleus is described by individual collisions of that particle with nuclear protons and neutrons. Such binary collisions are considered to be caused by the same forces as those responsible for scatterings from free protons and neutrons. Certain restrictions, however, may be imposed to differentiate between bound and free collisions. For example, scattering elastically from a spin-zero nucleus forbids spin flip, and thus the coefficients G and H in Eq. (5) do not contribute to the scattering. Because of our lack of information on the fundamental nucleon-nucleon interactions at this energy, the direct-interaction model is of little value in predicting details of the nucleon-nucleus scatterings.

B. Optical Model

In the optical model, the nucleus is represented by a complex potential well. Originally, this was a purely phenomenological model and was used to predict differential, absorption, and total cross sections. With the discovery of polarization effects, the potential was extended by Fermi to include spin-orbit coupling.[13] The work of Riesenfeld and Watson[19] has shown how the optical-model potentials can be related in a quantitative manner to the nucleon-nucleon phase shifts. In general, the radial dependence of the real and imaginary parts of this potential may be different. However, several authors have used the form

$$V(r) = V_e \rho'(r) - |V_c| e^{i\theta_c} \rho(r) + |V_s| e^{i\theta_s} \frac{\hbar}{\mu c} \frac{1}{r} \frac{d\rho(r)}{dr} \vec{\sigma} \cdot \vec{L}, \qquad (6)$$

where V_e is the Coulomb potential arising from the charge distribution $\rho'(r)$, and $\rho(r)$ is the nuclear distribution. The subscripts c and s refer to the central and spin-orbit parts of the potential. The arguments θ are not to be confused with the polar scattering angle. The imaginary part of the central nuclear potential can be related to the mean nucleon-nucleon total cross section for incident protons by[19]

$$\text{Im } V_c(r) = -\frac{k}{2E} A \bar{\sigma} \rho(r) ,$$

where E is the total energy of the proton in the proton-nucleus c. m. system, k is its c. m. momentum, A is the atomic number of the target particle, $\rho(r)$ has been normalized to unit volume integral

$$\int_0^\infty \rho(r) \, 4\pi r^2 dr = 1 ,$$

and

$$\bar{\sigma} = \frac{Z \sigma_{pp} + (A - Z) \sigma_{pn}}{A} .$$

The Born approximation allows insight into the role of the parameters that concern polarization. Although more sophisticated models yield better agreement with experiment, the numerical values of the parameters remain quite similar to those yielded by the Born approximation. Happily, the polarization in that approximation is independent of the shape of the nuclear density and can be written as[19]

$$P = \frac{2\chi P_{max}}{1 + \chi^2} .$$

Here we have used

$$P_{max} = \sin(\theta_c - \theta_s) ,$$

and

$$\chi = \left|\frac{V_s}{V_c}\right| \left(\frac{k_{lab}}{\mu c}\right)^2 \sin \theta_{lab}$$

where μ is the pion rest mass.

We note that the maximum polarization depends only on the relative phases of the central and spin-orbit potentials. The sine of the laboratory angle at which this maximum occurs is found by letting χ equal unity.

Using the optical model,[20] Batty has completed a comprehensive work on the subject of scatterings of high-energy nucleons by carbon. He has solved for radii and potentials, using experiments from 95- to 970-MeV incident proton energies. Because of this wealth of information, these data were analyzed along the lines of his formulation of the optical model.

For the nuclear distributions, the same shapes as found by Hofstadter in electron-scattering experiments were used.[21] For the light elements, a modified Gaussian was used:

$$\rho(r) = \left[1 + f\frac{4}{3}\left(\frac{r}{a_1}\right)^2\right] e^{-(\frac{r}{a_1})^2} .$$

Here the value of f determines the shape of the nuclear distribution,, and a_1 determines its size. The value $f = 0$ was used for helium, reducing the distribution to a pure Gaussian. For beryllium f was set to 1/2, and for carbon f was 1. The Fermi shape

$$\rho(r) = \frac{1}{1 + e^{[(r - r_0)/a]}}$$

was also used for carbon and for the heavier elements. Here r_0 is the radius at half height and a determines the thickness of the edge of the nucleus. To relate potentials with different radial forms, Feshbach suggests integrating over the volume of the nucleus and comparing results for the integral

$$I(V) = \int_0^\infty V(r) \, 4\pi \, r^2 \, dr.$$

While the modified Gaussian was used, the charge density was assumed to have the same distribution as the nuclear distribution. When the Fermi model was used, the trapezoidal model:

$$\rho'(r) = 1, \text{ for } r < (r_0 - 2.75\,a)$$

$$\rho'(r) = \frac{\left(r_0 + 2.75\,a\right) - r}{5.5\,a}, \text{ for } (r_0 - 2.75\,a) \leq r \leq (r_0 + 2.75\,a)$$

$$p'(r) = 0, \text{ for } r > (r_0 + 2.75\,a)$$

was used for the charge distribution.[21] The advantage here was that this form was analytically integrable. Its use was justified by the good approximation it makes to the Fermi model and also because the Coulomb effect is relatively unimportant at this energy. The equations relating these potentials to the differential cross section and the polarization by use of the Klein-Gordon equation and the WKB approximation are found in Appendix A.

III. EXPERIMENTAL METHOD AND EQUIPMENT

A. Background

The differential cross section $I_0(\theta)$ may be experimentally determined by observing unpolarized particles scattered into a detector subtending a solid angle $d\Omega$ by a target containing ρ particles per unit area. We can write

$$I_0 = \frac{N_1}{N_0 \, \rho \, d\Omega} \, ,$$

where N_1 is the number of particles scattered into the detector from an incident beam N_0, and

$$\rho = \frac{N \, d \, t}{A} \, .$$

Here N is Avagadro's number, and A, d, and t are the atomic number, density, and thickness of the target.

The polarization of high-energy scatterings is generally determined by a combination of two elastic scatters. Scattering an unpolarized proton beam from a target produces a polarized beam of scattered particles. Scattering again from a second target produces an asymmetry in the intensity which is given by Eq. (4),

$$I(\theta, \phi) = I_0(\theta) \left[1 + \epsilon(\theta) \cos \phi \right] \, .$$

By sampling the differential cross section at $\phi = 0$ and 180 deg, we may simply evaluate

$$\epsilon(\theta) = \frac{I(\theta, 0°) - I(\theta, 180°)}{I(\theta, 0°) + I(\theta, 180°)} \tag{7}$$

If both the first and the second targets are similar and both scatterings elastic, with the angles of scattering and the incident energies nearly equal, the asymmetry is the square of the polarization. The foregoing applies only to elastically scattered particles; if inelastic scatterings are included, the analysis is considerably more complex

(see Appendix B). The elasticity of each scattering can be ensured by imposing an energy requirement after the scatterings by range or magnetic analysis. This analysis need only be done after the second scattering, since if the projectile is still at full energy, apart from ionization and kinematic losses, it must have lost no energy at either the first or the second targets.

Once the polarizing or analyzing power, A, of a target for a particular angle of scattering has been found, then other polarization measurements may be made by changing one of the target materials or angles of scattering and again measuring the asymmetry:

$$P_{unk} = \frac{\epsilon_{meas}}{A}$$

B. Polarization by Varying the Sense
of the First Scattering Angle

At proton energies of several hundred MeV, insuring the elasticity is a difficult problem. Measuring a particle's energy by its range suffers from range straggling, and a large loss of intensity. Furthermore, any method that looks only at the summation of all particles above some minimum energy rather than a display of particles versus energy (i. e., $d^2\sigma/d\Omega\,dE$) in the region of energies in question is easy prey to a small energy asymmetry in the beam. In particular this is true when only the most elastic particles are to be detected.[9] Since the energy lost in exciting the nucleus a few MeV is a very small part of the initial energy of the proton, only the most elaborate magnetic analysis can detect the difference between the elastically and almost-elastically scattered particles. For example, exciting the carbon atom to its first excited states of 4.4 MeV costs an incident 730-MeV proton only 0.39% of its momentum. Heavier elements have even lower-lying excited states. In order to detect momentum differences of this amount, of the order of a few million gauss-inches is required of the analyzer. With a magnetic analyzer this large, problems quickly develop concerning the right-left asymmetry. An analyzing system of this capacity

needs space and power, and great care must be exercised to ensure that solid angles involved remain constant for the left and right scatters.

Great practical advantage is gained by not requiring magnetic analysis on both the left and the right side of the second scatterer. Varying the sense of the first scattering angle and holding the second fixed yields an asymmetry which is theoretically equivalent to varying the second and holding the first fixed. By fixing the angle of scattering after the second target, we can use a single fixed magnetic system; thus we gain convenience.

More significant than the practical advantage, however, is the freedom from systematic error that such a second-angle-constant system affords. If we monitor the beam at the second target, the asymmetry reflects in the first approximation the polarizing power of the first target and the analyzing power and the differential cross section at the second target. Since polarization is a slowly varying function of angle but the differential cross section varies strongly with angle, we are much more sensitive to alignment at the second target than the first target. Keeping an angle fixed affords the best way to keep it constant.

It may also be noted that to first order the first moments in the beam's position, angular, and energy distributions at the first target yield no false asymmetries. A complete treatment of misalignments and their effects on the measured polarization is given in Appendix C.

C. Beam-Transport System

The optical system external to the cylcotron shielding is shown in Fig. 1. This compound system can be decomposed into three units. The first unit contained two bending magnets which steered the beam through the first target at a given angle. The first magnet bent the beam away from the axis, and the second bent it back so that it crossed the axis at the first target. By increasing the current in the magnets,
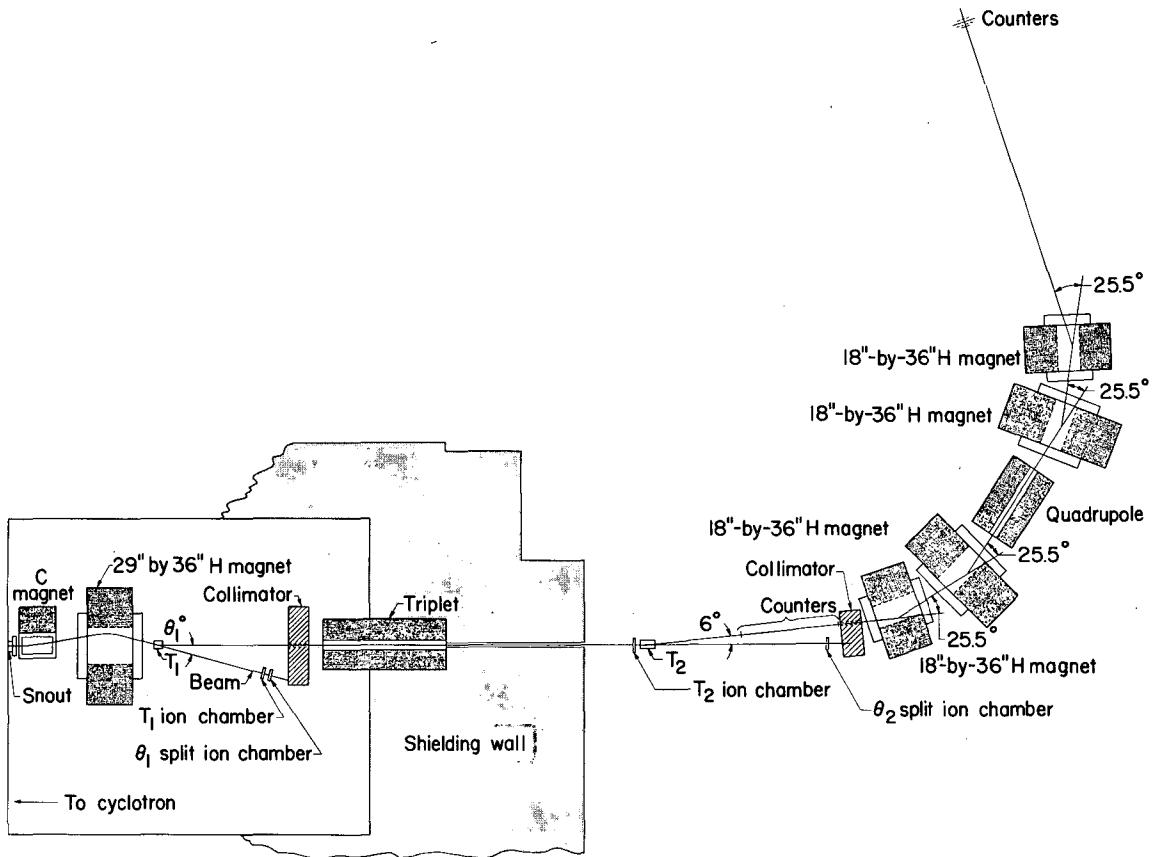
Fig. 1. Beam layout.

the angle of scatter was increased. A left angle of scattering is shown in the figure. To achieve a right scattering, the currents in the two bending magnets were reversed. Angles θ_1 from ± 4 to ± 13 deg were achieved by using the 29-by 36-in. H magnet shown in the figure. Near the end of the experiment, this magnet was replaced by a highly efficient 18-by 36-in. H magnet which allowed angles up to ± 20.5 deg. While this narrower magnet was able to achieve high flux to permit a greater angle of bend, it had to be repositioned sideways as the sense of the first scattering angle was reversed.

Preceding the snout shown in Fig. 1, out of which the beam emerges from the cyclotron shielding enclosure, are certain "internal" beam-transport and defining elements. By using a particular setting of the internal collimating jaws, the internal steering magnet, and the internal quadrupole, a beam of approximately 2.5×10^{10} protons per second was made incident on the first target in a spot about 1.5-in. diam. This spot had an intense central core about 1.0-in. diam. It might also be noted that a 2-by 2-in. collimator was used at the snout to remove the so-called satellite beam and other unwanted stray particles. A collimator was also used on both sides of the first target, T_1, for scattering at angles less than 5 deg. This prevented particles scattered at small angles from the snout collimator and the atmosphere upstream of the first target from traveling into the collimator shown in Fig. 1, and toward the second target, and greatly reduced the first-target-out subtractions.

In the second unit of the beam-transport system was a 16-in.-thick lead collimator and a quadrupole triplet. The collimator hole was 1-in. wide by either 2 or 4-in. high depending on the angle θ_1. For angles less than 6 deg, the shorter opening was used in order to restrict the angle ϕ in Eq. (4) to near ± 90 deg. For 6 deg and larger angles, the taller opening was used. The geometrical rms resolution in θ_1 was ± 0.36 deg for the solid targets. The angular blurring from multiple scattering must be added to this value. Protons scattering from the

liquid targets, because of their extended thickness, had an apparently wider source at the first target. Thus the definition in θ_1 depended on θ_1 and reached a maximum rms value of ± 0.65 deg for a scattering of 20.5 deg.

The quadrupole triplet simply focused the first target on the second target with near unit magnification in both the vertical and horizontal planes. It was run in a converging-diverging-converging fashion in the vertical plane in order to keep the protons out of a high magnetic field perpendicular to their direction of polarization. (A perpendicular field rotates the spin vector as well as the momentum.) The values for the currents were originally predicted by the IBM 7090 program OPTIK.[22] During the experiment these currents were varied, and the focus at the second target explored by a beam profile monitor. The optimum values were quite near those predicted.

Behind the triplet was a shielding wall, with a 2-3/4-in.-wide vertical slit which did not act as an aperture stop except for extreme rays coming from the liquid target when scattering at angles greater than 13 deg. A calculated 10% of the beam hit the wall for the largest angle of scattering, 20.5 deg.

The final unit contained another collimator and a large magnetic spectrometer. The collimator had a hole 2-in. wide and 4-in. high. The geometrical resolution in θ_2 depended on the size of the image spot at the second target, which in turn depended on whether there was a solid or a liquid target at T_1. Because of the projection of the scattered beam from the liquid 6-in. target at T_1, scattering at large angles from the liquid made the image at the second target larger. In addition the 12-in.-long liquid target at T_2 added to the lack of definition in θ_2. Thus, for solid targets at T_2, the geometrical resolution was ± 0.38 deg for solid targets at T_1. It reached a maximum of ± 0.54 deg in scattering at the maximum θ_1 angle of 20.5 deg from the liquid target at T_1. For the liquid targets at T_2, the angular resolution was ± 0.46 deg for solid targets at T_1, and reached a maximum of ± 0.59 deg for liquid targets.

The spectrometer was composed of four 18-by 36-in. H magnets with a focusing quadrupole in the center. Although physically the quadrupole was a doublet, it was used as a singlet converging in the horizontal plane. All vertical focusing was introduced by the fields of the bending magnets. The demand for a focus in the horizontal and vertical planes imposes two conditions. The two degrees of freedom are the current in the quadrupole and the location of the final focus. The overall magnification was again slightly higher than unity in both planes. In order to reduce aberrations, the bending magnets were shimmed to make $\partial \int \mathrm{Hd}\ell / \partial y$ more nearly equal a constant, where $\int \mathrm{Hd}\ell$ is the integrated magnetic field along the path of a particle, and y is the transverse horizontal direction. Making $\partial \int \mathrm{Hd}\ell / \partial y$ a constant can be interpreted as demanding that the field of the magnet be equivalent to that of a perfect wedge. The focusing properties were checked by use of wire-orbit techniques. During the experiment the current in the quadrupole was varied and observed to produce a best focus at the same value as that given by the wire orbits. The dispersion created by the system amounted to 1 MeV/cm at the final focus position. This value was given both by wire orbits and also by degrading the beam a known amount and observing it change position at the final focus. During the experiment, the spectrometer was adjusted for energy losses due to recoil and ionization at both targets. (When background was measured with the targets empty, only the difference in ionization losses was taken into account in readjusting the spectrometer.) The quadrupoles were adjusted only for protons scattering at angles greater than 13 deg from hydrogen.

The angle of scattering at the second target was fixed at 6 deg because it was estimated to best fit the following criteria: (a) a large ratio of elastically scattered protons from carbon and helium to inelastically scattered protons; (b) a large value for the product of $I(\theta)P(\theta)^2$; and (c) large polarization. The reasons for choosing these criteria are respectively to minimize (a) the error due to almost-elastic scatterings

(see Appendix B); (b) the statistical error; and (c) the systematic error. (Before the experiment the proton-carbon polarization at 6 deg was estimated on the basis of previous work to be about 50% [11,20].)

A helium atmosphere was used to reduce multiple scattering from the snout to the first target, inside the triplet quadrupole, and throughout the magnetic spectrometer. The beam size and shape at the final focus after the spectrometer were due almost entirely to energy spread in the cyclotron beam and the effects of inelastic scatterings in the targets.

D. Targets

A variety of targets was selected to span the whole range of atomic weights. In choosing particular targets, two criteria were employed. The target should be predominately composed of one isotope, and it is preferable that nuclear spin be zero. The group of elements selected by Chamberlain et al.[9] fulfills these criteria as much as any group, and in addition allows comparisons with energy on the same elements. These were hydrogen, helium, beryllium, carbon, aluminum, calcium, iron, and tantalum.

The liquid-hydrogen and helium target assemblies were similar to others used previously at this Laboratory and are described in detail in Ref. 23. The target flasks were cylinders with slightly domed ends, with their axes aligned with the line between the first and the second targets. Both were 6 in. in diameter so that all particles in the beams would interact with nearly the same amount of liquid despite the domed ends of the cylinders. The first target was only 6 in. long so that the scattering beam would not project too large an area. Because of the fixed small angle of scattering at the second target, the length of the second target was allowed to increase to 12 in.

E.   Detectors and Measurements

As seen in Fig. 1, the angle θ_1 was defined by the collimator, an ion chamber with the signal foil split, and the position of the first target.   The current from both halves of this ion chamber were moni- tored by electrometers and balanced on a zero-centered recording potentiometer.   The chamber rode on an arm which pivoted from a point directly below the first target and was positioned with the aid of two meter sticks which were fixed describing an arc.   The beam was positioned by the first two bending magnets so that the mode of the trans- verse intensity distribution of the beam was within 1/20 in. of this θ_1 split ion chamber.   It was known that the beam passed through the first target by the reading of the θ_2 second split ion chamber, which reflected the first target position through the quadrupole triplet.   This was experi- mentally shown by temporarily placing a split ion chamber by the first target and observing the balance in the θ_2 split ion chamber for both left and right scattering at the first target.   We note that the angle θ_1 is not affected, to first order, by a slight error in the position of the beam at the first target, since the split ion chamber and the collimator were substantially equidistant from the target.

This second split ion chamber also defined θ_2, the angle of scattering at the second target.   Again note that a small error in posi- tion at the second target causes no error in the angle θ_2.   The split ion chamber was mounted on a remotely controlled movable platform.   This enabled us to displace the chamber $\pm 1/20$ in. or 1 min of arc as defined from the second target, and observe the imbalance on the zero-centered potentiometer.   With the sensitivity determined thus, the electrometer scales were selected such that a beam displacement of comfortably less than 1/20 in. at θ_1 or θ_2 would sound an alarm requesting retuning of the first two bending magnets.

The initial beam that passed through the first target was meas- ured with an ion chamber filled with helium.   The current from this ion chamber did not depart from linearity by more than 10% at maximum

beam, and was integrated in the usual way by employing an electrometer and recording potentiometer. The flux of particles passing through the second target was again measured by an ion chamber. This ion chamber responded to a varying extent to particles of different energies leaving the first target. Since particles of lower energy deposit more energy in ionization, the signal from the chamber is disproportionately large for particles of lower energies. However, particles of a lower energy are focused in a shorter distance than those of full energy, and thus we find the shielding wall after the triplet acting to degrade, scatter, and stop particles of lower energy. What percent of these particles are scattered back into the channel, and how much ionization energy they deposit in the chamber are indeed complicated questions. A curve assuming no rescattering is presented in Fig. 2 and represents only a lower limit of the relative response vs particles of a given energy produced at the first target. Another curve shown in the figure was calculated on the assumption that only half the particles which strike the wall rescattered into the channel but were not degraded. A more elaborate calculation was not deemed warranted because of its difficulty and the tenuous nature of its assumptions, and because the percentage of particles starting from the first target with less than 600 MeV is thought to be small. This percentage is thought to be small because research done elsewhere[24] suggests that almost all protons from proton-nucleus scattering lose less than 100 MeV in small-angle scattering. An unfortunate exception is proton-proton scattering.

The ion chambers were calibrated relatively by putting them both in the main beam after the first target. Their absolute efficiency was calculated on the basis of an average of 25.5 eV per ion pair produced in argon.[25] The particles scattering elastically from the first and second target at the proper angles θ_1 and θ_2 were seen by two scintillation counters situated just after the second target, and an array of eight counters at the final focus. All of these eight were at least 10-in. high and contained all the beam in the vertical direction. There
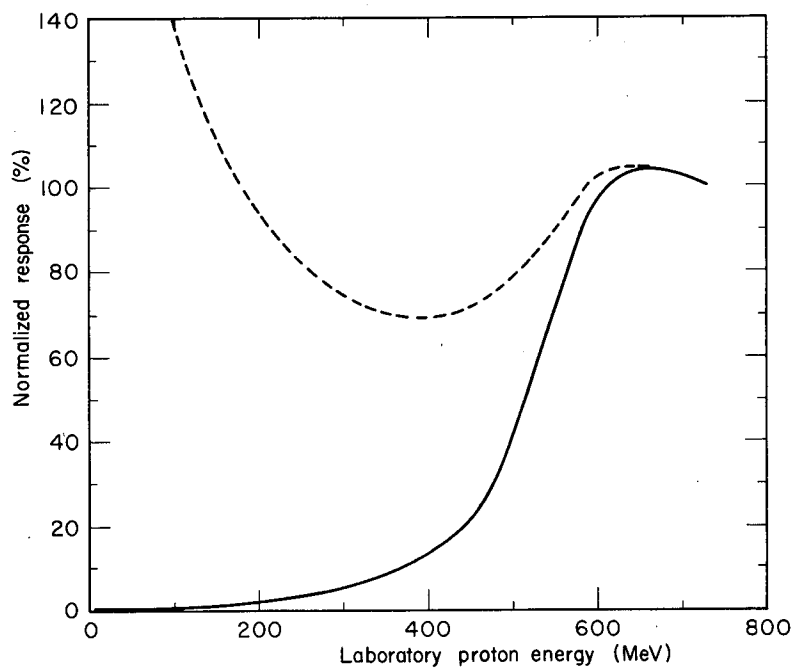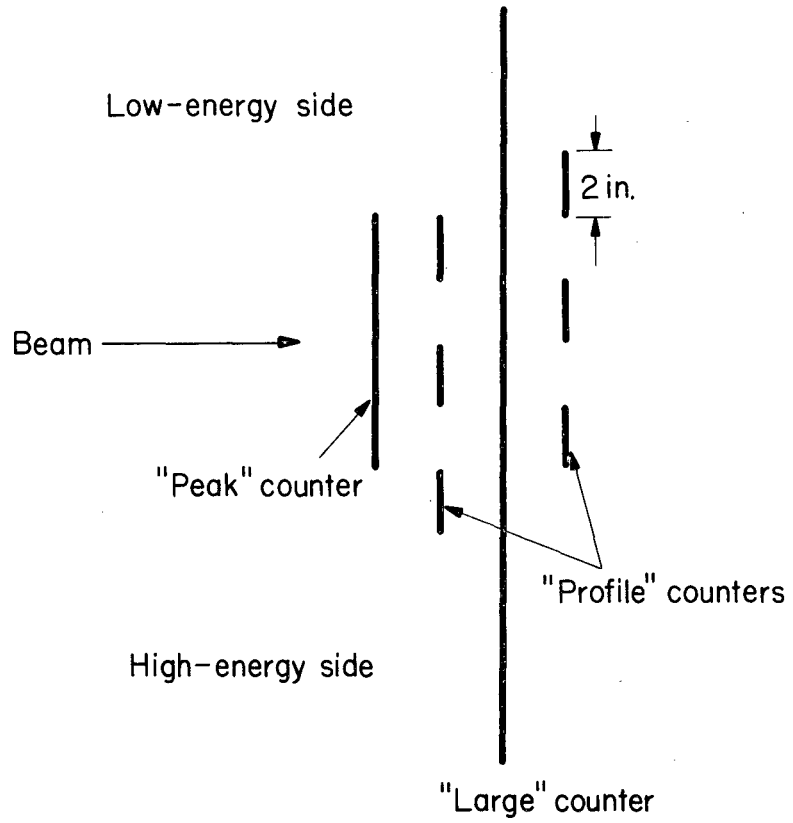
MU-30093

Fig. 2. Normalized response of the second-target ion chamber
to particles of a given energy leaving the first target. The
solid line is for no rescattering by the wall. The dashed
line is for half the particles rescattering with no loss of
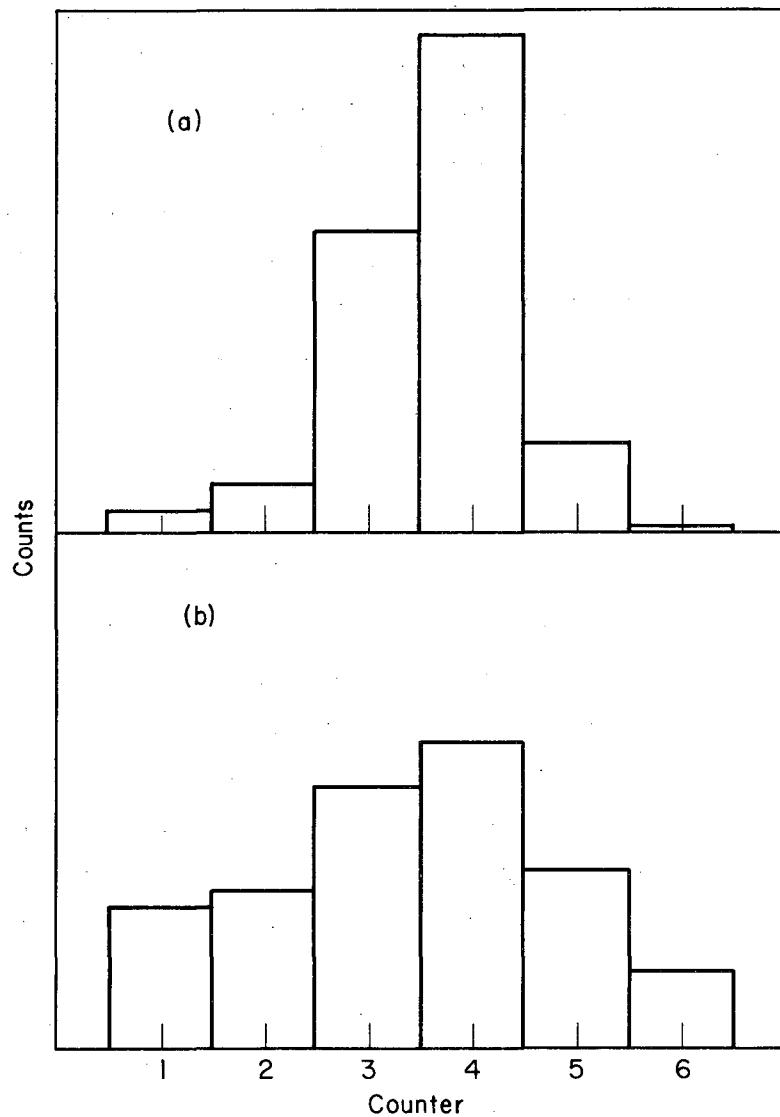energy.

was one large counter that subtended 24-in. horizontally, six small counters subtending adjacent 2-in. widths in the center of this large one, and one 8-in. counter that subtended the center four 2-in. counters. The counter positions are shown in Fig. 1, and an enlargement of the final array is shown in Fig. 3. With standard electronic circuits,[26] a coincidence was first made between the two upstream counters and the large counter at the final focus. This output was then used further to produce secondary coincidences formed between it and the other seven members of the array. In this manner the profile of the beam was continuously monitored as well as the number of particles in the center peak of the beam. Much attention was paid to maximizing the number of particles in this "peak" counter, thus making sure that this number was not subject to variation as the currents in the magnets drifted slightly. It was originally hoped that polarization could be obtained as a function of energy loss, independently in each of the six 2-in. counters. The steepness of the beam distribution together with the regulation of the magnets made this impossible. The counting rate in the high-energy side of the array varied by an order of magnitude in less than 2-in. A variation in the magnet currents amounting to one part in 10,000 caused the counting rate in the highest channel to vary by 25%. The beam distribution was not symmetric with energy but fell less sharply on the low-energy side because of the original energy distribution from the cyclotron and because of contributions from inelastic states. The distribution found at the final focus is shown in Fig. 4 for scattering through both 3 and 13 deg at θ_1 and with carbon at both the first and second targets.

The polarization of the peak of the elastic--near-elastic distribution was measured. This included in general from 5 MeV above the peak to 15 MeV below the peak. At angles for which this peak was due mainly to elastically scattered protons, protons which lost more than 15 MeV were completely excluded. However, when the near-elastics themselves contributed substantially to this peak, then near-elastics losing up to about 20 MeV were allowed to register in this

Fig. 3. Final counter array.

MU- 30092

Fig. 4. Beam profile after spectrometer for (a) $\theta_1 = 3$ deg, and (b) $\theta_1 = 13$ deg. Each counter subtends 5 MeV. Protons scatter from carbon at T_1 and T_2. Counter 6 is on the high-energy side.

MU-29175

"peak" counter. Also measured was the polarization of the entire group of particles in the large 24-in. counter. This included about 30 MeV above and below the elastically scattered particles. The polarization of these two groups never differed by more than their statistical error, but at angles larger than the diffraction minima, the polarization was consistently lower for the group including to 30-MeV loss.

Asymmetries ϵ were calculated by taking a percentage difference of a ratio of particles registering in the peak or large counters to the particles passing through the second-target ion chamber for both left and right scatterings at the first target:

$$\epsilon = \frac{\left(\frac{C}{T}\right)_{LL} - \left(\frac{C}{T}\right)_{RL}}{\left(\frac{C}{T}\right)_{LL} + \left(\frac{C}{T}\right)_{RL}} \quad ,$$

where C is the flux of particles in the counters and T is the normalized current in the ion chamber at the second target. The ratio of the second ion chamber to the first ion chamber remained constant to within 2% as the first angle was reversed. This is a check on the reproducibility of the first angle, as it reflects directly the differential cross section of the first target. Target-out subtractions for both targets were taken into account by normalizing to the number of particles passing through the first-target-ion chamber.

Additional ratios involving these same fluxes may be interpreted as differential cross sections. The ratio of the ion chamber flux in the second target to that in the first target is a measurement of the elastic, near-elastic, and to an uncertain extent the inelastic differential cross section. This is uncertain because of the response of the second-target ion chamber as shown in Fig. 2.

The ratio of the flux, C, in the "peak" or "large" counters to the flux, M, in the first-target ion chamber, is proportional to a product of elastic plus near-elastic differential cross sections at the two targets:

$$(C/M)_{ave} = \frac{d\sigma}{d\Omega_1} \frac{d\sigma}{d\Omega_2} \, d\Omega_1 \, d\Omega_2 \, \rho_1 \, \rho_2 \, .$$

In order to not include polarization effects, an average value for both left and right scattering at the first target must be used. Since a product of cross sections is involved, answers obtained from this latter method reflect only one-half of the constant systematic errors. This is easily seen when both target conditions are similar, since one takes the square root of the intensity to find the cross section. Errors in the ion-chamber calibration and in the solid angles are reflected only in the cross section through the square root:

$$\left(\frac{d\sigma}{d\Omega}\right) = \left(\frac{(C/M)_{ave}}{d\Omega_1 \, d\Omega_2 \, \rho_1 \, \rho_2}\right)^{1/2} \, .$$

When one target is changed, the ratio of the unknown $d\sigma/d\Omega$ to that of the "known" $d\sigma/d\Omega$ is related by the formula

$$\frac{\left(\dfrac{d\sigma}{d\Omega}\right)_{unk}}{\left(\dfrac{d\sigma}{d\Omega}\right)_{kn}} = \frac{\left(\left[(C/M)_{ave}\right]_{meas} \Big/ \rho_{unk}\right)}{\left(\left[(C/M)_{ave}\right]_{kn} \Big/ \rho_{kn}\right)} \, .$$

The ratio is seen to be independent of all constant systematic errors, and the unknown differential cross section is seen to reflect only the systematic errors in the "known" differential cross section.

IV. RESULTS AND DISCUSSION
A. General Accuracy and Reproducibility

Throughout this experiment a great premium was placed on accuracy of the polarization measurements. The most important measurement is the one in which the analyzing power of the second target is established. The use of helium as an analyzer is conceptually pleasing because of its lack of excited states. However, comparison of the energy distribution of the protons scattered at 6 deg by carbon at both targets with that of protons scattered by helium at both targets showed no evidence of almost-elastic scattering at 6 deg. Because of the convenience gained by working with a target that is solid at room temperatures, this double-carbon, 6-deg scattering was then accepted as a standard for the experiment and was repeated over 20 times and under all conditions. Measurement showed that polarization was not detectably affected by changes in the beam shape, beam intensity, beam spill, or thickness of the targets. The system was further checked by comparing measurements where both targets were hydrogen, helium, beryllium, or aluminum with measurements where either target was replaced by carbon. All measurements were consistent. The agreement in the case of helium and carbon is shown along with the helium data in Table III. Because of its lack of excited states, most asymmetries were measured with helium as an analyzer. To increase counting rates, however, carbon was generally used as an analyzer for asymmetries (second target) on hydrogen, helium, and scattering at 10 and 13 deg from the solid targets. The analyzing power of carbon at 6 deg was found to be 0.300 ± 0.003, and that of helium was 0.333 ± 0.003. Since all polarization measurements were reproducible to within their statistical errors, and there was no reason to suspect a constant systematic error, the errors reported with the data are those due to statistics.

Another check was accomplished by accelerating alpha particles and double-scattering them. Since the alpha's have no spin, any measured asymmetry reflected a bias in the experiment. This check

is much more sensitive to misalignment, since the differential cross section versus angle is varying more rapidly than in the proton-carbon case. To increase the flux, an angle of 4 deg was used for the first angle of scattering, and tantalum as the first target. Carbon was used as a second target. Although the beam shape was similar to the proton beam shape at the first target, no strong elastic peak after the two scatterings was found at the final focus. This was probably due to a relative increase of inelastic scatterings and possibly to a greater initial momentum spread of the beam at the first target. Alignment of the alpha beam was less certain than that of the proton beam, because of the low flux of particles at the θ_2 split ion chamber. Despite these problems, the asymmetry was found to be $1.5 \pm 1.5\%$. Because of the more rapid change of differential cross section with angle for alpha's, this result affords a great deal of confidence in the system.

Differential-cross-section data were obtained as a byproduct of the polarization measurements. The experimental design was opti - mized for polarization results. To yield polarization measurements ion-chamber multiplication factors and solid angles need only remain constant as θ_1 is reversed, and the absolute counting rate need not be normalized. Perhaps the largest error in the differential-cross-section measurements came through use of collimators rather than counters to define solid angles. This was particularly troublesome in absolute measurements regarding the second ion chamber, since it reacted to particles of all energies. It is particularly difficult to estimate the number of particles scattering down the collimator. No allowance for collimator scattering has been made. This probably causes the differ- ence between the ion-chamber differential-cross-section results at small angles on intermediate-mass targets and the elastic differential cross sections as measured by the counters and the first ion chamber. This ion-chamber ratio varied some $\pm 10\%$ throughout the experiment, although it did not vary during any series of measurements by more than 2%. The ratio of the counters to the first ion chamber was repro- ducible to about $\pm 5\%$. The statistical error was always less than 1%.

The rms multiple-scattering angle when combined with the geometrical rms angular resolution yields the total angular resolution. The total angular resolution in θ_1 and θ_2 is given in Table I. The lack of resolution means that an average over an angular region rather than a specific point has been recorded. Since the polarization generally is a slowly varying function of angle, this does little to change the results. However, the differential-cross-section results are higher--at least before the diffraction-minimum angles are approached--than would have been measured with a better resolution.

Table I. Root-mean-square angular resolution in θ_1 and θ_2 for measurements of various elements.

| Element	θ_1 or θ_2	θ_{rms} (deg)		
		(geometrical)	(multiple scattering)	(combined)
H	1	0.36 to 0.65	0.11	0.38 to 0.66
He	1	0.36 to 0.65	0.12	0.38 to 0.66
He	2	0.46 to 0.59	0.17	0.49 to 0.61
Be	1	0.36	0.27	0.45
C	1	0.36	0.33	0.48
C	2	0.38 to 0.54	0.39	0.55 to 0.67
Al	1	0.36	0.53	0.64
Cu	1	0.36	0.58	0.68
Fe	1	0.36	0.57	0.67
Ta	1	0.36	1.02	1.07

B.   Results

1.   Protons on Hydrogen

Protons inelastically scattered from hydrogen do not affect the measurements of the polarization and elastic differential cross section on hydrogen, since it takes more than 150 MeV to produce a pion at this incident energy.   At 4.5 and 6 deg the contribution from "target-out" in the counters was more than that due to the hydrogen.   However, the background fell off rapidly with angle so that by 10 deg its contribution was down to less than 5%, and of course presented no problem at larger angles.   The data in Table II and Fig. 5 are from the large counter.   The peak counter registered an artificially high polarization value; the reason is discussed in Appendix C.

Table II.   Polarization and differential cross section
for protons scattering from protons.

θ_{lab} (deg)	P	ΔP	$(d\sigma/d\Omega)_{lab}$ (mb/sr)	
			(elastic)	(ion-chamber ratio)
4.5	0.250	0.013	59.6	116
6.0	0.354	0.012	57.6	112
7.3	0.392	0.010	53.3	105
8.6	0.431	0.012	48.3	96
10.0	0.483	0.009	47.8	92
11.5	0.553	0.013	41.0	88
13.0	0.572	0.007	40.7	91
15.3	0.609	0.008	35.1	59
16.4	0.652	0.015	30.0	48
18.0	0.661	0.009	29.0	48
20.5	0.666	0.010	23.6	38
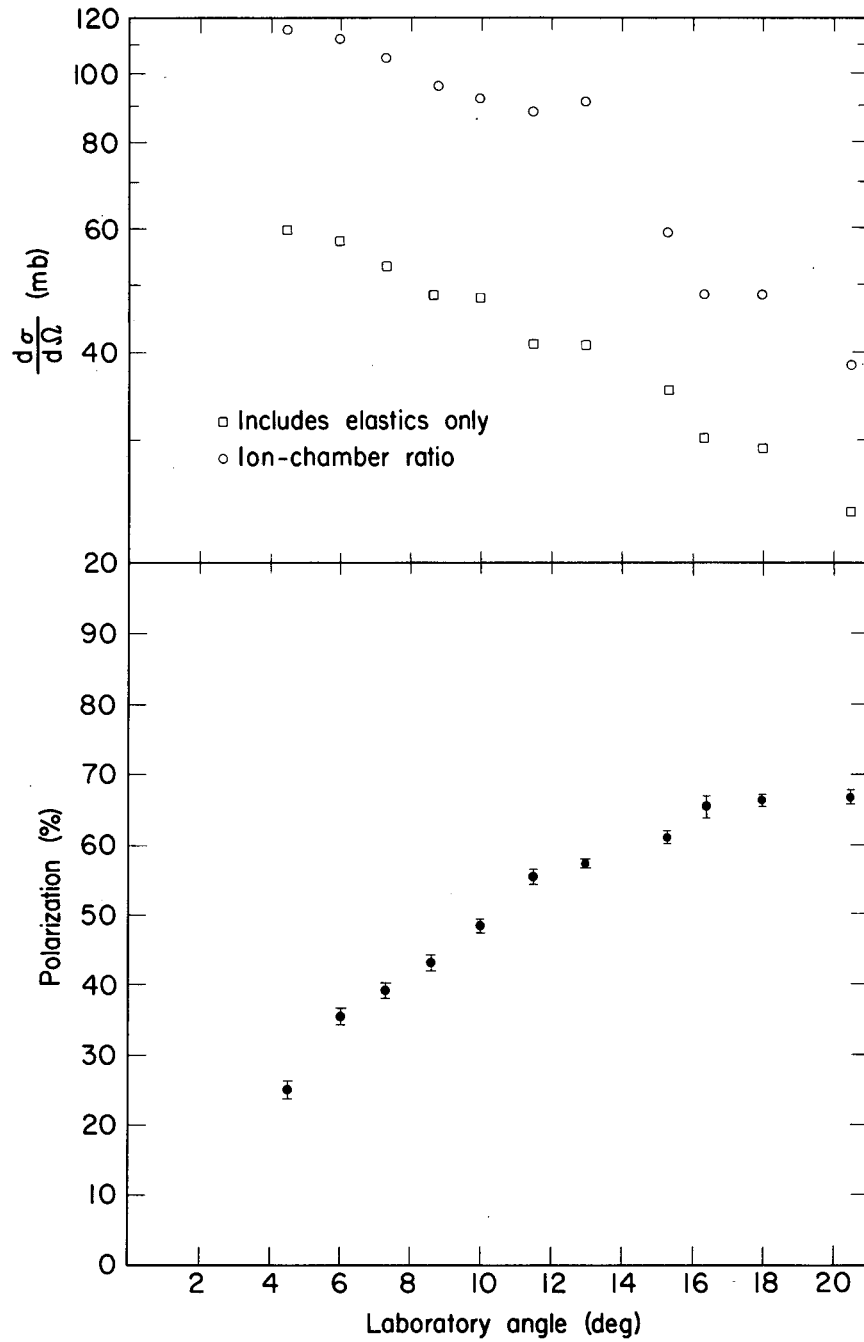
Fig. 5. Differential cross section and polarization vs angle for protons on protons at 735-MeV incident lab energy.

MUB-1737

In scattering 20.5 deg from hydrogen, 118 MeV is lost in recoil. The differential cross section and the analyzing power of carbon for protons scattering at 6 deg at the second target must then be modified to take into account this energy loss. The values used are given in Appendix D. Notice that for the wider angles of scattering from hydrogen, the polarization accuracy is limited by the present lack of definite knowledge of the analyzing power of carbon at energies less than 730 MeV.

Because of the uncertainty in the differential-cross-section data there is little new information from it. The large value of the ion-chamber ratio compared to the elastic differential cross section reflects the fact that the "inelastics" are more strongly peaked forward in the lab system than are the "elastics." Notice that, as the angle is increased, the proportion of inelastics drops. Polarization is remarkably large, and this is the most interesting result of the experiment.

2. Protons on Helium

The differential cross section and polarization for protons scattering from helium are given in Table III and plotted in Fig. 6. The polarization data here and in the following tables is from the peak counter. Only in the hydrogen and helium measurements do almost-elastics not seriously distort the polarization and differential-cross-section measurements. The minimum energy a proton can lose in an inelastic collision is the 20 MeV necessary to remove one nucleon, so there was no almost-elastic contamination in the elastic-peak measurements. Particularly noticeable are the very large differences between the ratio of the ion chambers and the elastic differential cross section, as determined from the ratio of counters to the first ion chamber. Here as with all other elements except hydrogen, the proportion of inelastics increases with angle. No diffraction effects are visible in the differential cross section, but the polarization is clearly headed downward as the angle is approached at which one would expect the first diffraction minimum. These features are similar to the data at 310 MeV.[9]

Table III. Polarization and differential cross section
for protons scattering from helium

θ_{lab} (deg)	P	ΔP	$(d\sigma/d\Omega)_{lab}$ (mb/sr)		
			(elastic)	(includes 30-MeV loss)	(ion-chamber ratio)
4.5	0.280	0.012	360	366	554
6.0	0.332	0.005	280	291	473[a]
6.0	0.339	0.005	273	288	-[b]
6.1	0.328	0.008	260	267	432
7.3	0.369	0.011	200	210	361
8.6	0.393	0.011	145	152	299
10.0	0.423	0.010	96.0	103	227
11.5	0.413	0.013	55.4	61.1	185
13.0	0.439	0.018	31.5	35.1	143
13.0	0.446	0.018	32.5	39.4	146[a]
15.3	0.348	0.033	10.6	12.9	103
16.4	0.265	0.043	5.4	7.0	91
18.0	0.132	0.072	2.0	2.7	76

[a]Both targets helium

[b]Carbon at the first target, helium at the second.

3. Protons on Beryllium and Carbon

The beryllium and carbon data are given in Tables IV and V
and plotted in Figs. 7 and 8. At small angles, the beryllium and carbon
polarization data look quite similar to the helium data. From the energy
profile at the final counters for the measurements at 10 and 13 deg, it
is clear that the results are an average over almost-elastic states and
are not to be interpreted as elastic measurements. An elastic polari-
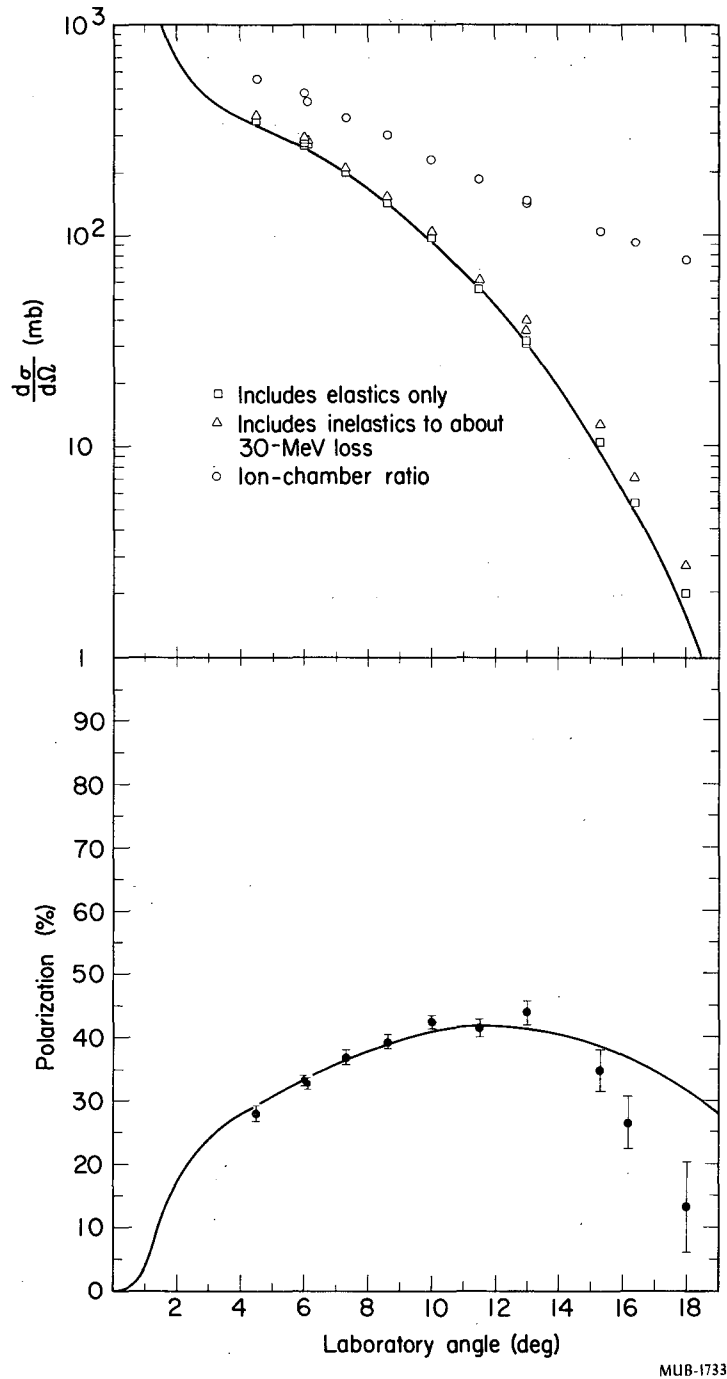zation, which closely follows that of the helium polarization as the angle

Fig. 6. Differential cross section and polarization vs angle for protons on helium at 730-MeV incident lab energy. The curves are the result of the optical model for elastic scattering with the potentials and radial values given in Table X.
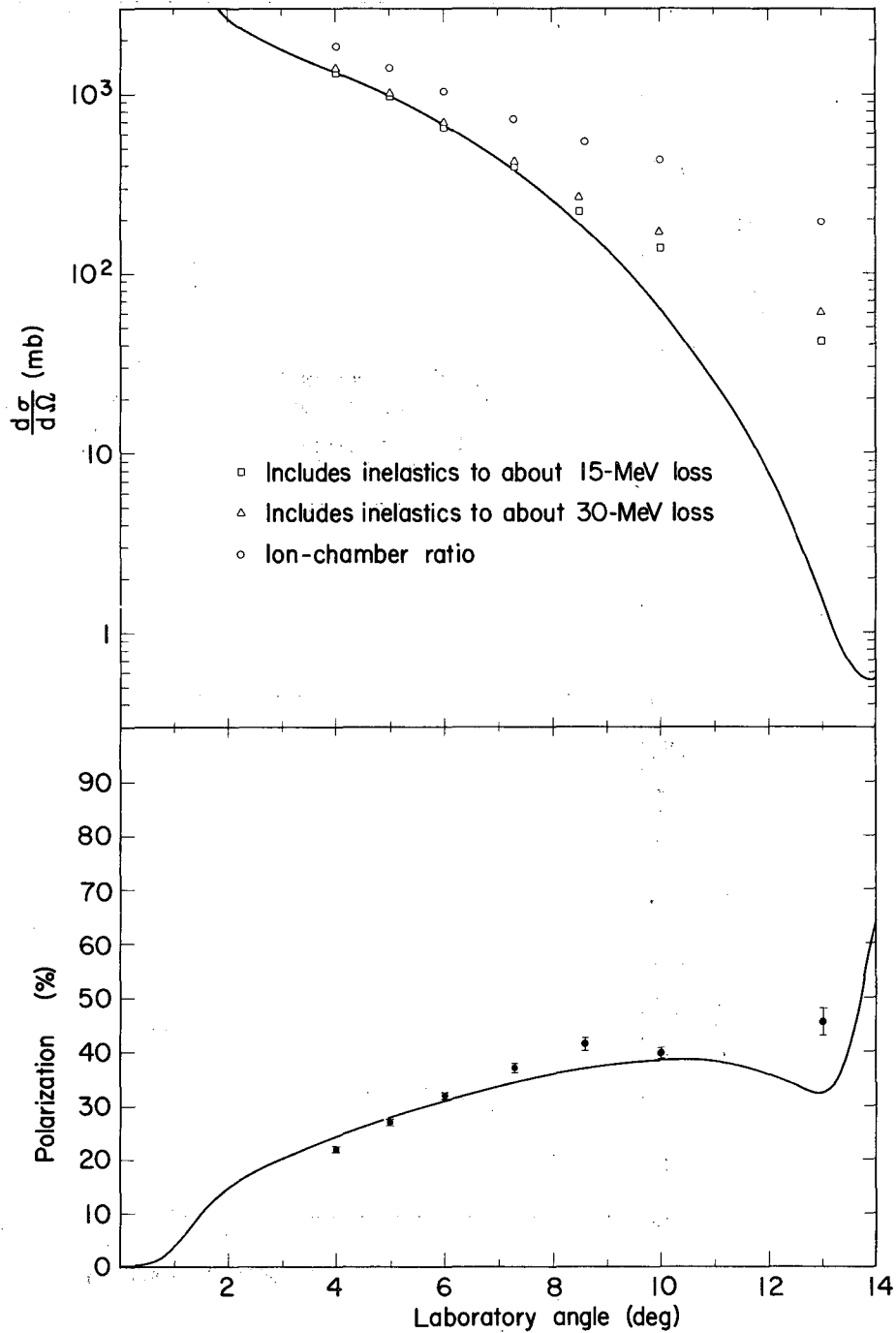
Table IV. Polarization and differential cross section
for protons scattering from beryllium

θ_{lab} (deg)	P	ΔP	$(d\sigma/d\Omega)_{lab}$ (mb/sr)		
			(includes 15-MeV loss)	(includes 30-MeV loss)	(ion-chamber ratio)
4.0	0.217	0.007	1320	1390	1830
5.0	0.267	0.007	951	1005	1390
6.0	0.316	0.007	640	692	1020
7.3	0.368	0.008	381	428	718
8.6	0.411	0.012	223	266	541
10.0	0.395	0.010	137	169	424
13.0	0.452	0.025	41	60	291

Table V. Polarization and differential cross section
for protons scattering from carbon

θ_{lab} (deg)	P	ΔP	$(d\sigma/d\Omega)_{lab}$ (mb/sr)		
			(includes 15-MeV loss)	(includes 30-MeV loss)	(ion-chamber ratio)
4.0	0.233	0.005	2120	2210	2820
5.0	0.265	0.005	1500	1580	2090
6.0	0.300	0.003	970	1040	1450
7.3	0.348	0.006	520	570	920
8.6	0.369	0.009	250	300	610
10.0	0.335	0.015	116	148	440
13.0	0.445	0.028	33	50	300

Fig. 7. Differential cross section and polarization vs angle for
protons on beryllium at 730-MeV incident lab energy. The
curves are the result of the optical model for elastic
scattering with the potentials and radial values given in
Table X.
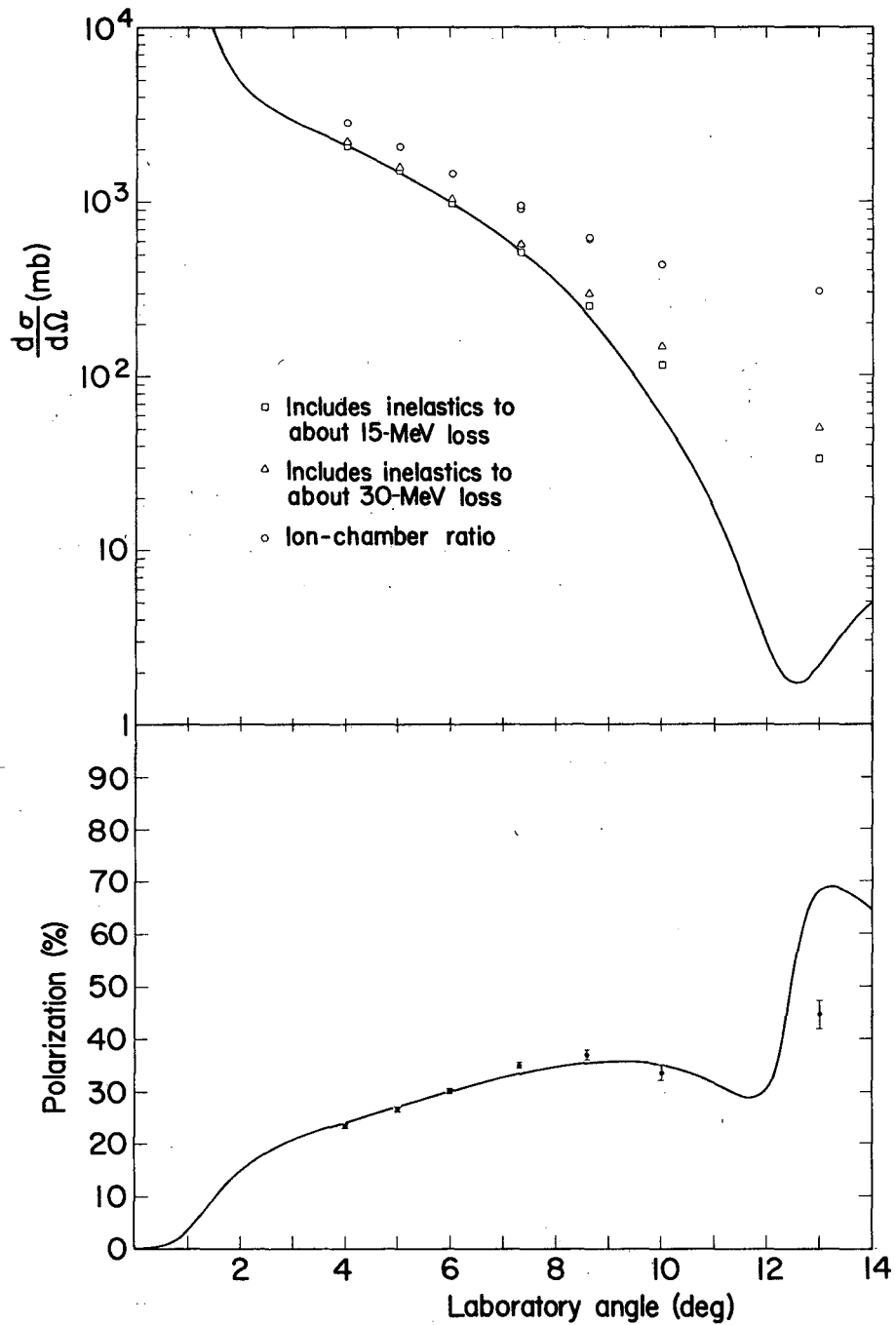
Fig. 8. Differential cross section and polarization vs angle for
protons on carbon at 730-MeV incident lab energy. The
curves are the result of the optical model for elastic
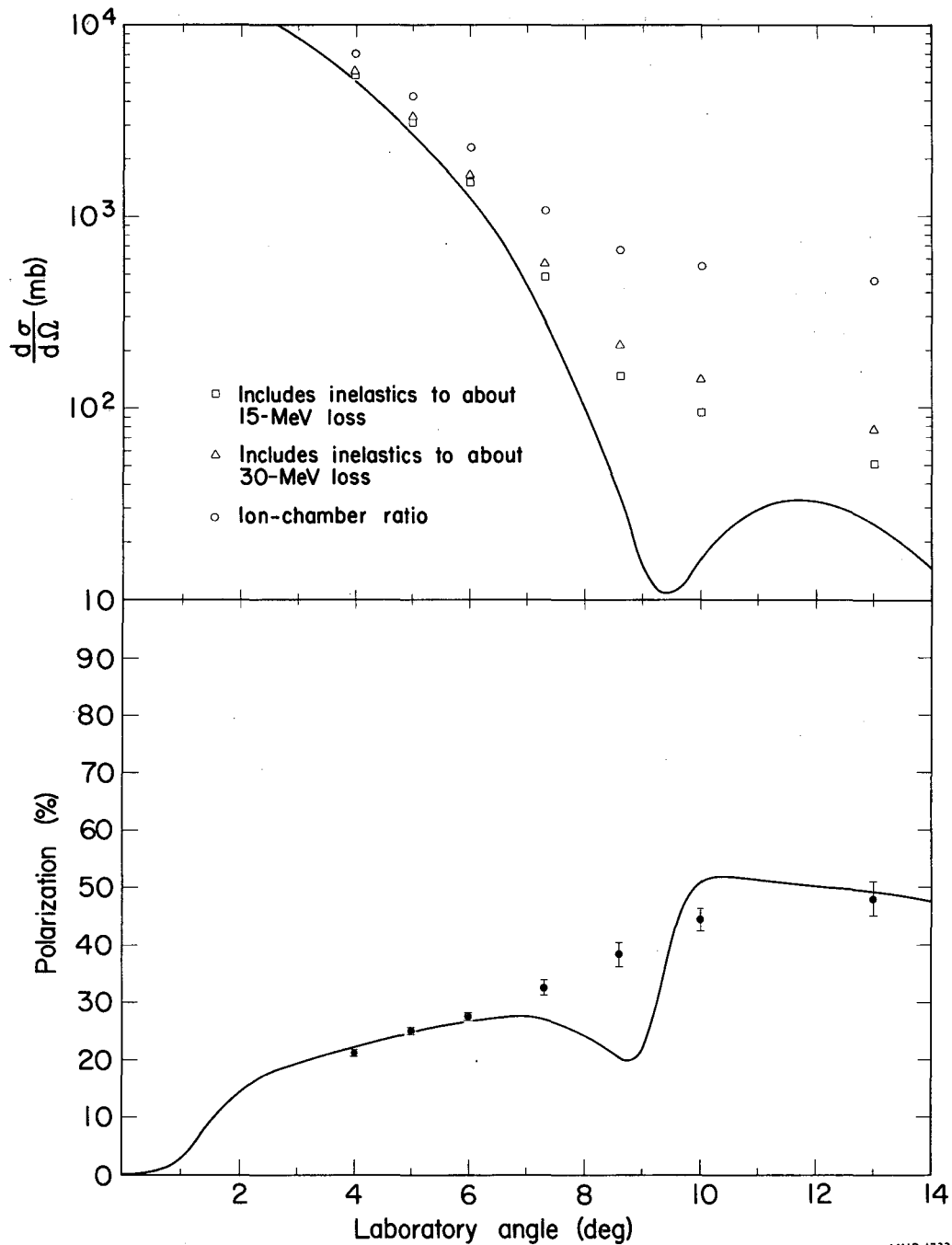scattering with the potentials and radial values given in
Table X.

MUB-1739

approaches the classical diffraction minimum, is not inconsistent with these measurements. The differential-cross-section results can be interpreted as only an upper limit for the elastic differential cross section at the larger angles.

4. Protons on Aluminum, Calcium, Iron, and Tantalum

The data concerning these elements are found in Tables VI through IX, and plotted on Figs. 9 through 12. The most striking feature of the polarization measurements are that they are so similar at the same laboratory angle. Almost-elastics also contaminate the results whenever the elastic diffraction minimum is approached. The angular resolution in the measurements of the heavier elements suffers because of multiple scattering. Because of these effects, fine details of the scatterings are unobservable. This is particularly true in the case of tantalum.
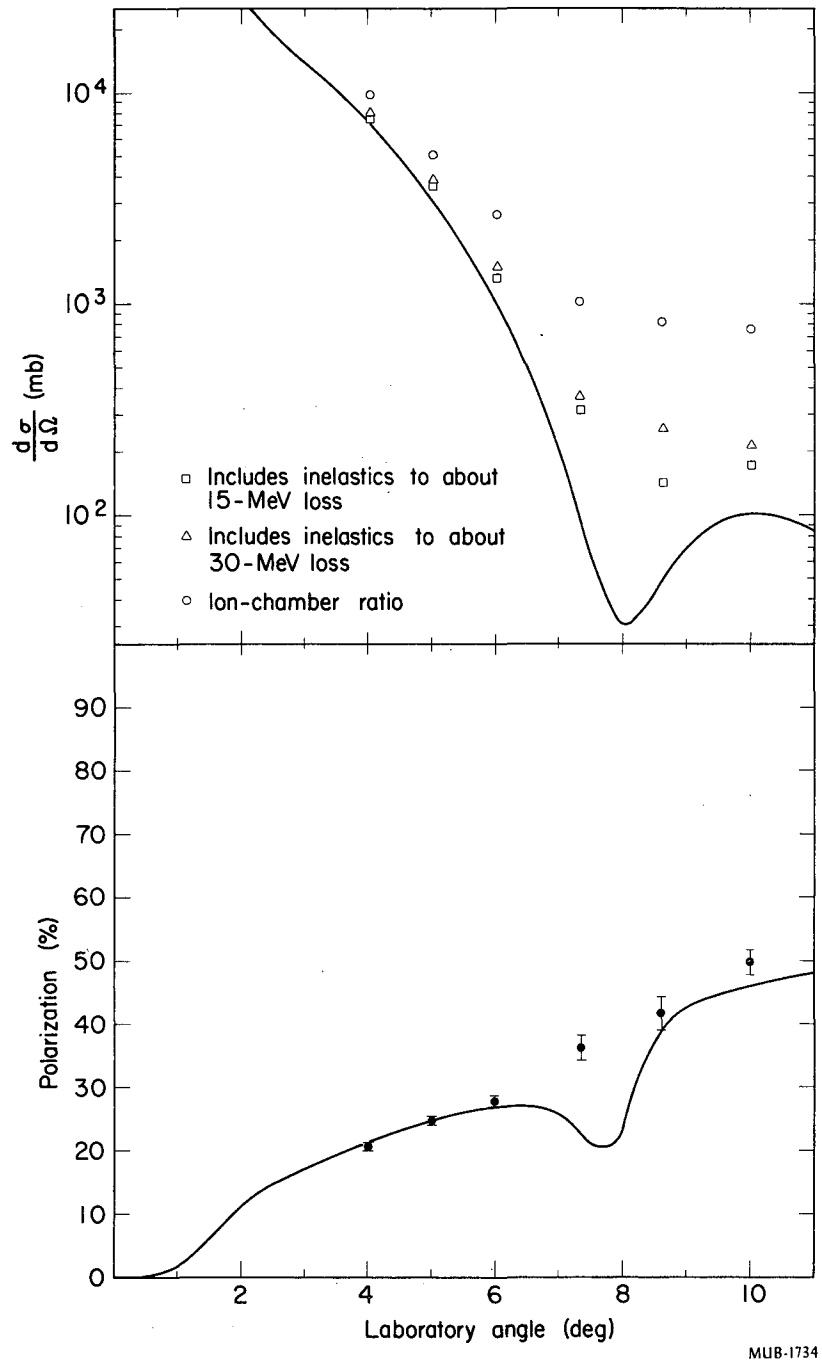
Table VI. Polarization and differential cross section
for protons scattering from aluminum

θ_{lab} (deg)	P	ΔP	$(d\sigma/d\Omega)_{lab}$ (mb/sr)		
			(includes 15-MeV loss)	(includes 30-MeV loss)	(ion-chamber ratio)
4.0	0.212	0.006	5480	5730	7089
5.0	0.250	0.008	3150	3320	4269
6.0	0.275	0.007	1510	1640	2304
7.3	0.326	0.013	491	577	1082
8.6	0.383	0.022	147	215	665
10.0	0.443	0.021	95.3	144	559
13.0	0.531	0.030	51.8	78.6	460

Fig. 9. Differential cross section and polarization vs angle for
Protons on aluminum at 730-MeV incident lab energy. The
curves are the result of the optical model for elastic
scattering with the potentials and radial values given in
Table X.

Fig. 10. Differential cross section and polarization vs angle for protons on calcium at 730-MeV incident lab energy. The curves are the result of the optical model for elastic scattering with the potentials and radial values given in Table X.
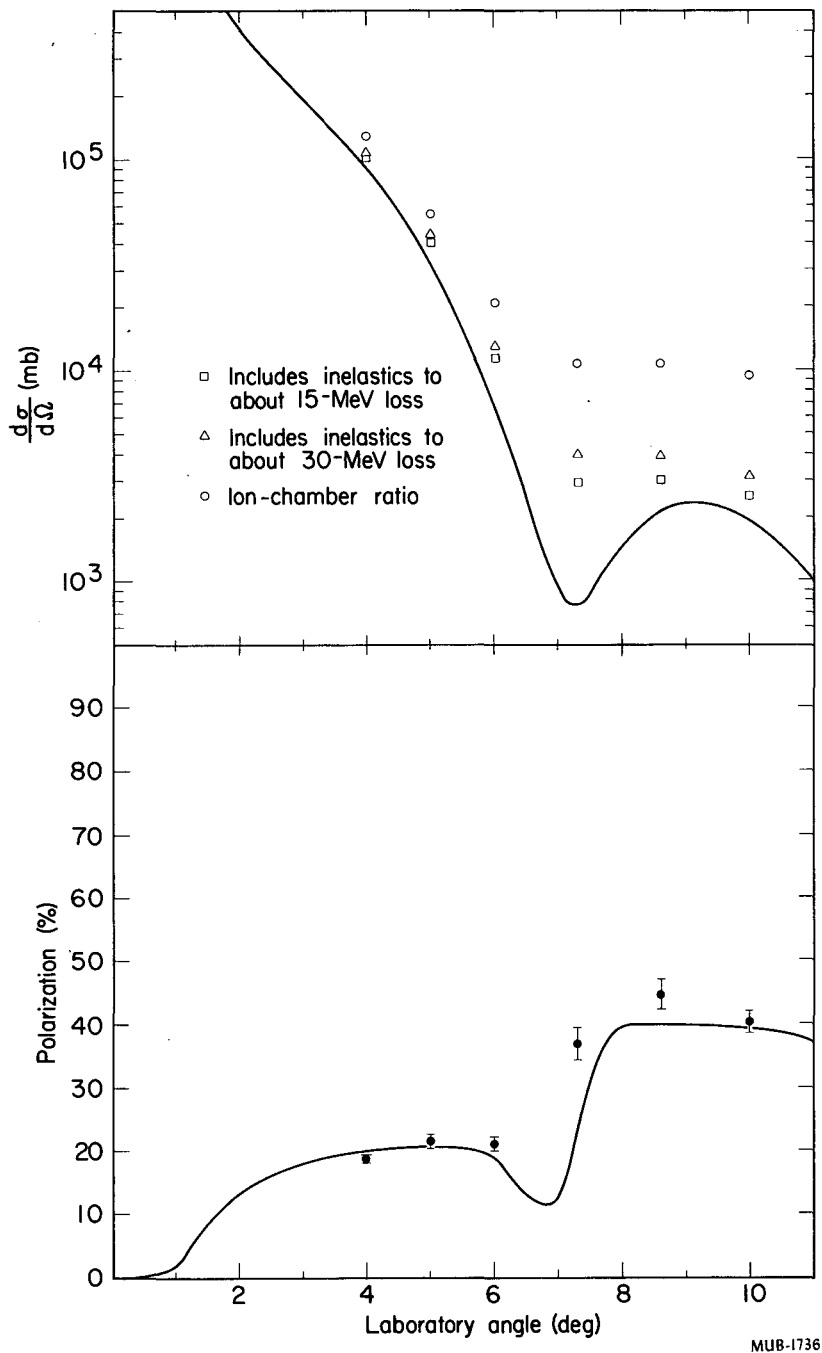
Fig. 11.   Differential cross section and polarization vs angle for
protons on iron at 730-MeV incident lab energy.   The
curves are the result of the optical model for elastic
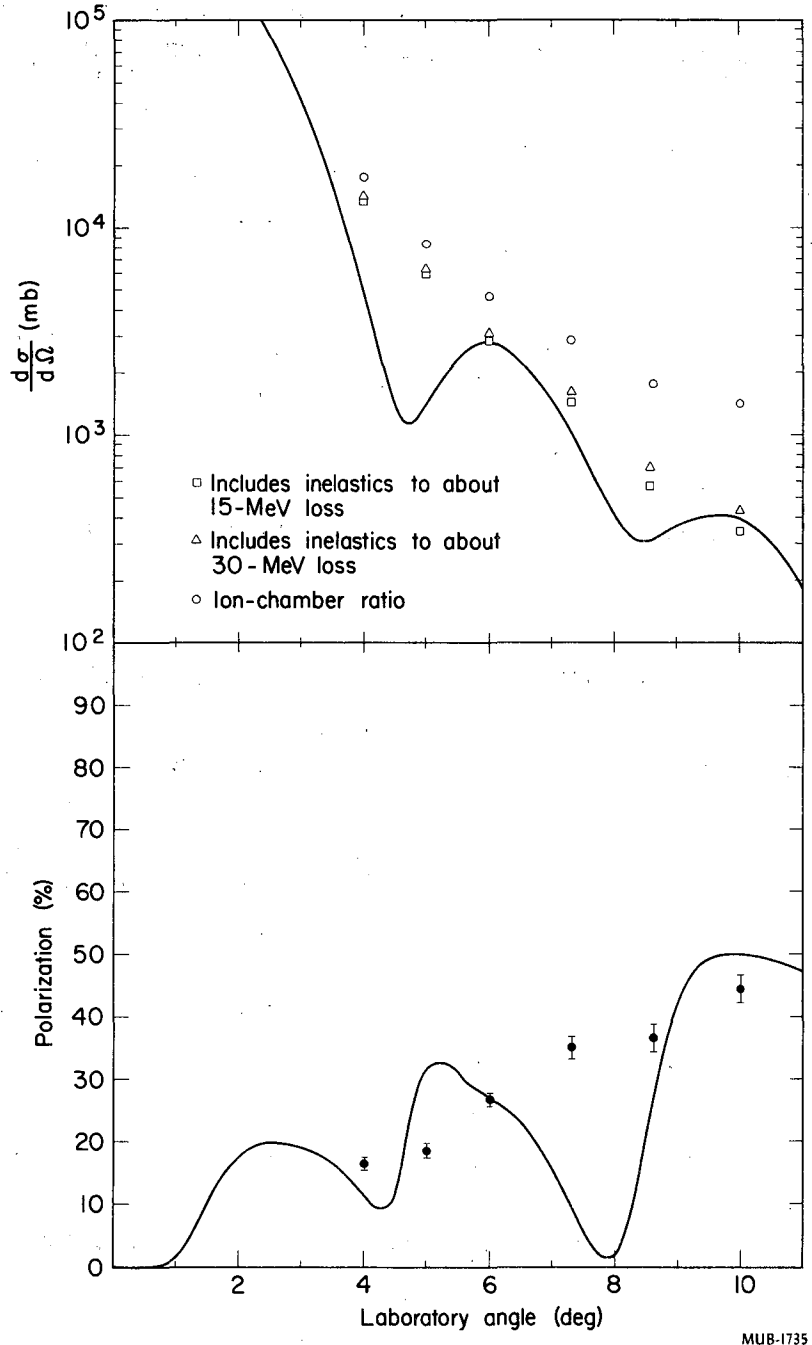scattering with the potentials and radial values given in
Table X.

Fig. 12. Differential cross section and polarization vs angle for protons on tantalum at 730-MeV incident lab energy. The curves are the result of the optical model for elastic scattering with the potentials and radial values given in Table X.

Table VII. Polarization and differential cross section
for protons scattering from calcium

θ_{lab} (deg)	P	ΔP	$(d\sigma/d\Omega)_{lab}$ (mb/sr)		
			(includes 15-MeV loss)	(includes 30-MeV loss)	(ion-chamber ratio)
4.0	0.205	0.006	7690	8040	9857
5.0	0.246	0.008	3680	3900	5028
6.0	0.278	0.009	1360	1505	2265
7.3	0.362	0.019	324	424	1020
8.6	0.416	0.027	142	259	829
10.0	0.497	0.020	174	237	777

Table VIII. Polarization and differential cross section
for protons scattering from iron

θ_{lab} (deg)	P	ΔP	$(d\sigma/d\Omega)_{lab}$ (mb/sr)		
			(includes 15-MeV loss)	(includes 30-MeV loss)	(ion-chamber ratio)
4.0	0.187	0.006	10080	10550	12769
5.0	0.215	0.011	3910	4170	5395
6.0	0.211	0.011	1113	1270	2041
7.3	0.369	0.026	285	386	1042
8.6	0.447	0.024	292	380	1038
10.0	0.403	0.018	245	308	909

Table IX. Polarization and differential cross section
for protons scattering from tantalum

θ_{lab} (deg)	P	ΔP	$(d\sigma/d\Omega)_{lab}$ (mb/sr)		
			(includes 15-MeV loss)	(includes 30-MeV loss)	(ion-chamber ratio)
4.0	0.164	0.011	13600	14300	17569
5.0	0.185	0.011	5980	6370	8408
6.0	0.266	0.011	2870	3130	4644
7.3	0.349	0.018	1440	1610	2849
8.6	0.365	0.023	570	707	1762
10.0	0.444	0.023	339	434	1401

C. Expansion of the Proton-Proton Data vs $\text{Cos}^2\theta$

The most interesting result of the experiment is the high polar-
ization found in the proton-proton scattering. This high value means
that there is a strong spin dependence to the nucleon-nucleon force in
the channel where the total isotopic spin is one. The fact that proton-
nucleus polarization is lower indicates that the proton-neutron polariza-
tion may be lower. It is certainly clear that the proton-proton and
proton-neutron total cross sections are different at this energy, and
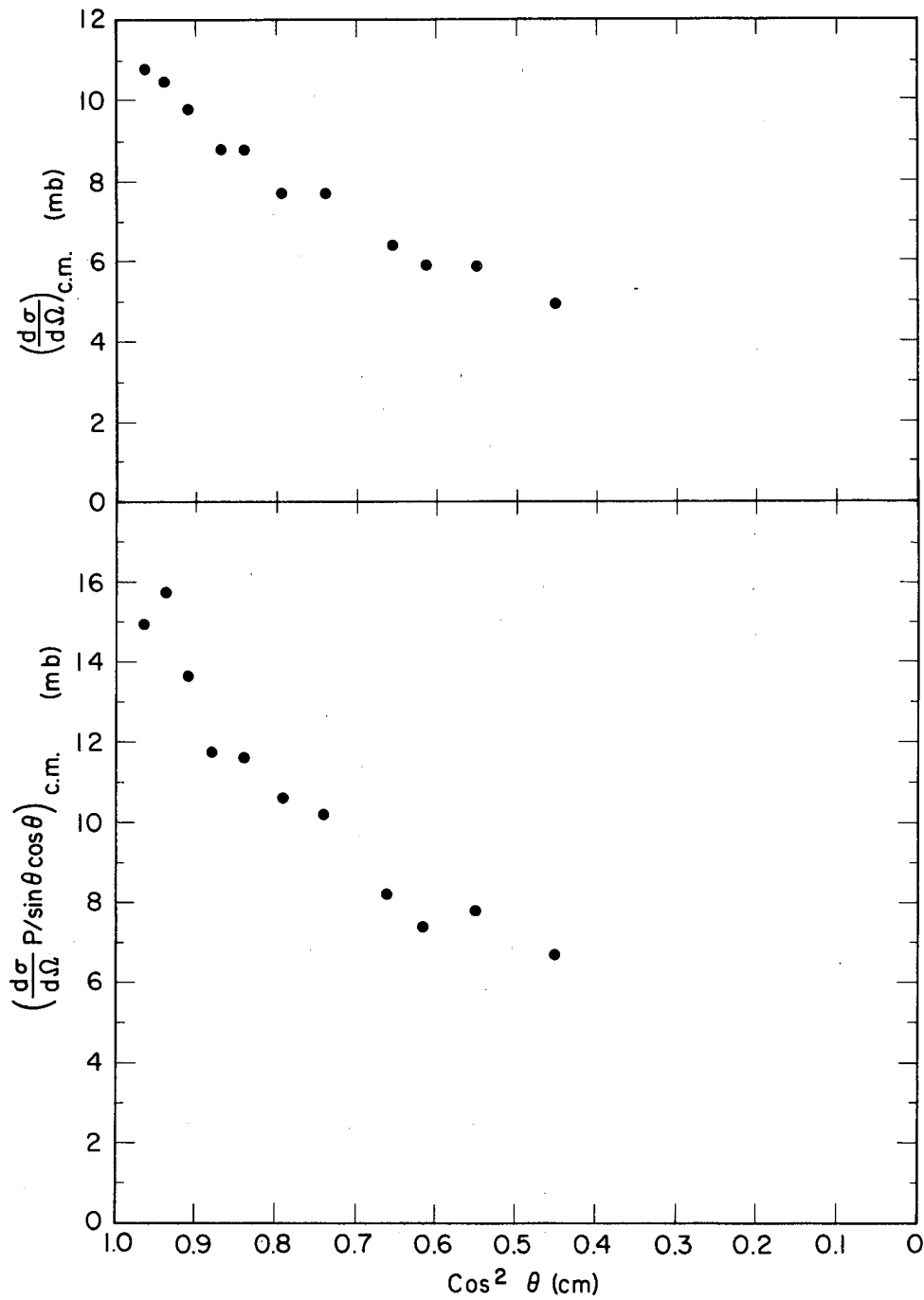we should not expect the polarization to be the same.

Some information as to angular-momentum states contributing
to the scattering can be obtained by plotting $I(\theta)$ and $I(\theta)P(\theta)/\sin\theta\cos\theta$
vs $\cos^2\theta$ in the c.m. system. Using the symmetry of the proton-proton
interaction, Wolfenstein has shown that the differential cross section
must be expandable in a power series of the form[27]

$$I(\theta) = \sum_{n=0}^{N} a_{2n} \cos^{2n}\theta \; ,$$

and the product of the differential cross section times the polarization
to be expandable in the form

$$\frac{I(\theta)P(\theta)}{\sin\theta\cos\theta} = \sum_{m=0}^{M} b_{2m} \cos^{2m}\theta \; .$$

If an expansion of the form $A + B \cos^2\theta$ is sufficient, then the data
should fall on a straight line. If the differential cross section at 90 deg
in the c.m. system is still in the neighborhood of 2 mb (as it was at
657 MeV[10]) or higher, the I vs $\cos^2\theta$ relationship in Fig. 13 definitely implies
that we need higher powers than $\cos^2\theta$. However, this only implies a
total angular momentum of more than one. A more significant conclu-
sion can be derived from the plot of $I(\theta)P(\theta)/\sin\theta\cos\theta$ vs $\cos^2\theta$,
which is also given on Fig. 13. The slope of the points again shows need
for higher powers than $\cos^2\theta$. This means that the $^3F_4$ state or higher
odd waves must play a significant role in the scattering. These conclu-
sions agree with results observed at 635 MeV[10].

Fig. 13. Plot of $(d\sigma/d\Omega)_{c.m.}$ and $(d\sigma/d\Omega)_{c.m.} P/(\sin\theta_{c.m.} \cos\theta_{c.m.})$ vs $\cos^2\theta_{c.m.}$ for protons on protons at 735-MeV lab energy.

D. Optical-Model Fitting

In fitting the experimental data with the optical model, an IBM 7090 computer program was used. This program started with the potential in terms of $|V_c|$, θ_c, $|V_s|/|V_c|$, and $(\theta_c - \theta_s)$, and with radial values for a_1 and f for fitting the modified Gaussian, or r_0 and a for fitting the Fermi form. From these it generated values of the polarization as well as the differential, total, and absorption cross section. These values were compared with the corresponding experimental values and χ^2 computed, where

$$\chi^2 = \sum_i \left| \frac{\left(\sigma_{exp}\right)_i - \left(\sigma_{cal}\right)_i}{\left(\Delta\sigma_{exp}\right)_i} \right|^2 .$$

The program then varied any or all of the first five of these parameters in a grid manner, attempting always to reduce χ^2.

Uniqueness is determined by starting the program at different initial values. The data are fit well by several choices of the phase of the central potential, θ_c. The solution with a large positive imaginary central potential and a small negative real central potential fits the data as well as any. In addition, Batty shows this solution to fit nicely with measurements at other energies.[20] It may be noted that the dip in the calculated polarization at the diffraction-minimum angle is much more pronounced for the solution having a small positive real central potential. Two families of solutions correspond to $\sin(\theta_c - \theta_s)$ being in the first and second quadrants. The corresponding real and imaginary parts of the spin-orbit potential are positive and negative, respectively. The positive solution fits the helium data better. Combining this with the fact that at lower energies the real part of the spin-orbit potential has been shown to be positive,[2] the positive solution was taken to be the correct family.

When the modified Gaussian was used for fitting data on the light elements, the value of the radius a_1 was allowed to vary; f, a, and r_0 were fixed at the values obtained by electron scattering. Because

of the lack of almost-elastic scattering contaminating the helium data, the potential values found in fitting this data are judged most reliable. In fitting the beryllium and carbon data, the data from only the first four angles was used because of the high percentage of contamination from almost-elastic states at larger angles. For carbon, in addition to the angular distribution and polarization data, the total and absorption cross sections were used. Moskalev et al. measured the absorption cross section for 650-MeV protons on carbon to be 227 ± 12 mb.[28] Booth et al. found the value 220 ± 18 mb for 765-MeV neutrons on carbon.[29] The value 225 ± 10 mb was used in our program. For the total cross section, Booth et al.[29] measured 342.1 ± 3.7 mb, and Dzhelepov et al.[30] measured 319 ± 2 mb for 590-MeV neutrons. We used a value of 330 ± 10 mb.

For the heavier elements the average proton-nucleon cross section $\bar{\sigma}$ and the ratio of real to imaginary central potential was fixed at the carbon values. Only the spin-orbit potential was allowed to vary. Data from only the first three angles were used. A search was not made for tantalum, but the average value of $\bar{\sigma}$ and the ratio of all potentials were held fixed. The values of the potential and related parameters are given in Table X. The errors included on the potentials are crudely estimated by seeing how χ^2 varied as these parameters changed. The polarization and differential cross sections are plotted along with the data on Figs. 6 through 12. The fit with the data is considered to be good when allowance is made for almost-elastic scattering and angular resolution. The central potential is seen to be mostly imaginary and the real part small and negative. [The reader is reminded of the minus sign in front of the central potential term in the conventional definition of the potential given in Eq. (6).] The phase of the spin-orbit potential is close to that of the central potential. This reflects the low values of the polarization. The predictions of the modified Gaussian and Fermi models for proton-carbon scattering were extremely similar. Those of the modified Gaussian are plotted in Fig. 8.

Table X. Optical-model parameters

Element	Model	$|V_c|$ (MeV)	θ_c (deg)	$|V_s|/|V_c|$	$(\theta_c - \theta_s)$ (deg)	Re V_c (MeV)	Im V_c (MeV)	Re V_s (MeV)	Im V_s (MeV)
He	Gaussian	63 ± 4	97 ± 10	0.052 ± .004	23 ± 2	- 7.6	62.2	0.90	3.14
Be	Mod. Gauss.	48 ± 3	100 ± 10	0.037 ± .004	27 ± 8	- 8.4	47.6	0.53	1.69
C	Mod. Gauss.	49 ± 3	100 ± 10	0.035 ± .004	26 ± 4	- 8.4	48.2	0.48	1.64
C	Fermi	56 ± 3	100 ± 10	0.035 ± .004	27 ± 4	- 9.6	55.2	0.59	1.86
Al	Fermi	54.8	100[a]	0.030 ± .004	29 ± 4	- 9.5	54.0	0.53	1.58
Ca	Fermi	51.1	100[a]	0.021 ± .004	46 ± 4	- 8.9	50.3	0.63	0.89
Fe	Fermi	53.2	100[a]	0.026 ± .004	31 ± 4	- 9.2	52.4	0.51	1.29
Ta	Fermi	46.0	100[a]	0.035[a]	27[a]	- 8.0	45.3	0.47	1.54

Element	Model	$\dfrac{I(\text{Re}V_c)}{A}$	$\dfrac{I(\text{Im}V_c)}{A}$	$\dfrac{|I(\text{Re}V_s)|}{A}$	$\dfrac{|I(\text{Im}V_s)|}{A}$	A
		(MeV - 10^{-39} cm^3)				(amu)
He	Gaussian	- 34	281	9	32	4.003
Be	Mod. Gauss.	- 52	294	6	21	9.013
C	Mod. Gauss.	- 57	330	8	22	12.011
C	Fermi	- 56	325	7	23	12.011
Al	Fermi	- 56	316	6	20	26.98
Ca	Fermi	- 55	313	8	12	40.08
Fe	Fermi	- 55	312	7	17	55.85
Ta	Fermi	- 54	309	7	22	180.95

Element	Model	f	$a_1/A_{1/3}$	a	$r_0/A_{1/3}$	$\bar{\sigma}$	σ_t	σ_a
			(10^{-13} cm)			(mb)		
He	Gaussian	0.0	0.93 ± .02	-	-	39 ± 3	116	90
Be	Mod. Gauss.	0.5	0.82 ± .02	-	-	38 ± 3	251	192
C	Mod. Gauss.	1.0	0.73 ± .02	-	-	42 ± 3	324	235
C	Fermi	-	-	0.50	0.98	42 ± 3	334	244
Al	Fermi	-	-	0.60	1.00	42[a]	649	454
Ca	Fermi	-	-	0.57	1.06	42[a]	891	598
Fe	Fermi	-	-	0.57	1.06	42[a]	1121	729
Ta	Fermi	-	-	0.64	1.14	42[a]	2813	1690

[a] Held fixed during analysis

E.   Comparison with Polarization Data at 635 MeV

Comparing this work with polarization in proton-proton scattering measured by Mescheriakov et al. at 635 MeV,[10] we find that while the shape of polarization with angle is quite similar, the value at the lower energy is lower, reaching a maximum of 42%.   At face value this indicates that the polarization has increased rapidly during this change of about 100 MeV.   On the other hand, the polarization in proton-beryllium scatterings is significantly higher at this lower energy.[11]   It is difficult to reconcile these two sets of data.   To have the proton-proton polarization increasing by 50% of its value while the proton-beryllium polarization is decreasing by 50% is indeed unusual, and difficult to explain on theoretical grounds.

A possible explanation is found by looking more closely at the reported polarization at 635 MeV.   The polarization of the beam was established by a double scattering from beryllium at 9 deg.   The elasticity of scattering was checked by a range telescope.   The reported polarization abruptly increases as the minimum energy passed by the range telescopes of the system nears that of the elastically scattered particles.   On the basis of the reported $d^2\sigma/d\Omega dE$ this polarization change with more lower-energy particles accepted in the telescopes is only possible if the inelastically scattered particles have an extremely large polarization which is opposite in sign to the polarization of the elastically scattered particles.   Because of the similarity of the elastic polarization and the inelastic polarization in this experiment, no justification of this type is plausible.

This rapid change of polarization with the lowest energy accepted and the high value of the most elastically scattered particles could be explained by a misalignment of the system due to an energy correlation across the position at the second target.   As seen in Fig. 1 of Ref. 11, the bending magnet between the first and second target places the highest-energy particles on the left side of the target.   These tend to scatter into the left telescope, since a smaller angle of scattering is required.   This would favor left-left type scatters rather than the

left-right variety and yield an anomalously large value for the "elastic" polarization. If a lower value for the proton-beryllium polarization is used, then a lower value must be used for the polarization of the beam which induced the asymmetry in the proton-proton polarization. Since the proton-proton asymmetry was measured by looking at both recoiling protons, we have no reason to believe that erroneously large asymmetries were recorded. Thus we must raise the values of the proton-proton polarization. This resolves the conflict.

ACKNOWLEDGMENTS

APPENDICES

A. Optical-Model Equations

In solving the relativistically valid Klein-Gordon equation in the W. K. B. approximation, we obtain

$$A(\theta) = \frac{k}{1} \int_{-\infty}^{\infty} J_0(kb \sin \theta) \left\{ \frac{e^{i\chi^+} + e^{i\chi^-}}{2} - 1 \right\} b\, db$$

and

$$B(\theta) = -\frac{k}{2} \int_{-\infty}^{\infty} J_1(kb \sin \theta) \left\{ e^{i\chi^+} - e^{i\chi^-} \right\} b\, db,$$

where we have used the convention that $\hbar = \mu = c = 1$, J_0 and J_1 are the zeroth- and first-order Bessel functions respectively, and b is the classical impact parameter defined by the diagram.

By χ^+ and χ^- we mean

$$\chi^{\pm} = \chi_c + \chi_e \pm \chi_s.$$
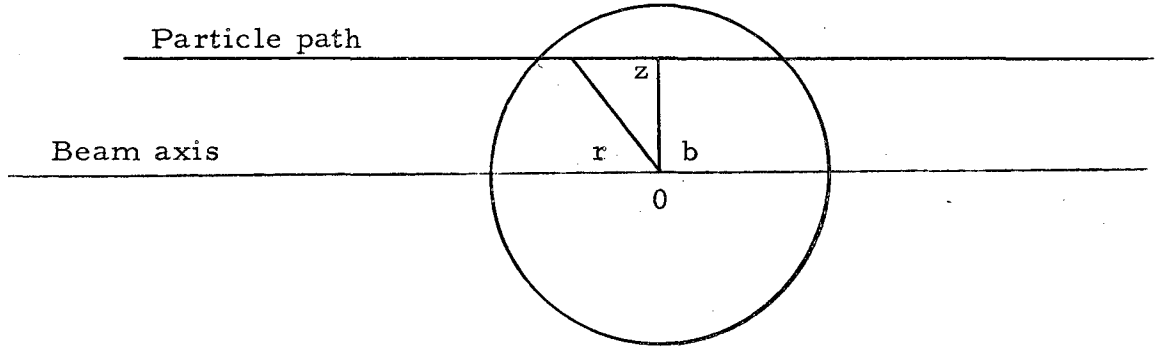
These χ's are defined as integrals over the potentials along the path of the particles:

$$\chi_c(b) = -\frac{E}{k} \int_{-\infty}^{\infty} V_c(r) dz,$$

where $V_c(r) = \left| V_c \right| e^{i\theta_c} \rho(r),$

$$\chi_e(b) = -\frac{E}{k} \int_{-\infty}^{\infty} V_e(r)\, dz \ ,$$

where $V_e(r) = za\rho'(r)$, and

$$\chi_s(b) = -\frac{E}{k}\, kb \int_{-\infty}^{\infty} V_s(r)\, dz \ ,$$

where $V_s(r) = |V_s| e^{i\theta_s} (1/r)[d\rho(r)/dr]$. The multiplicative kb in χ_s comes from the $\vec{l} \cdot \vec{s}$ in Eq. (6).

To take advantage of the short range of the nuclear forces in these integrals while at the same time handling the Coulomb force, we consider a distance R such that, for $r > R$,

$$\rho(r) = \rho'(r) = 0 \ .$$

Then we have

$$\chi_c = \chi_s = 0$$

and

$$\chi_e = \chi_p = -\frac{E}{k} \int_{-\infty}^{\infty} V_p\, dz \ ,$$

where p denotes the quantity is calculated assuming a point charge. The amplitude for a point charge is

$$A_p(\theta) = \frac{k}{i} \int_0^{\infty} J_0(kb \sin \theta) \left\{ e^{i\chi_p} - 1 \right\} b\, db \ .$$

From Mott and Massey we may write[23]

$$A_p(\theta) = -\frac{2y}{k \sin^2 \theta} \exp\left\{ i\left[-2y \ln \sin \frac{\theta}{2} - y \ln 2 + 2 \ \text{ang} \ \Gamma(1 + iy) \right] \right\} \ ,$$

where

$$y = \frac{E z a}{k} \; .$$

With this rearrangement we may now write

$$A(\theta) = \frac{k}{i} \int_0^R J_1(kb \sin \theta) \left\{ \frac{e^{i\chi^+} + e^{i\chi^-}}{2} - e^{i\chi_p} \right\} b\, db + A_p(\theta) \, ,$$

$$B(\theta) = -\frac{k}{2} \int_0^R J_0(kb \sin \theta) \left\{ e^{i\chi^+} - e^{i\chi^-} \right\} b\, db \, ,$$

and

$$\chi_e = \frac{2E}{k} \left\{ \int_0^\infty V_p(r)dz - \int_0^R V_p(r)dz + \int_0^R V_e(r)dz \right\} \, ,$$

where the first term is χ_p and is given by the formula[17]

$$\chi_p = \frac{2Eza}{k} \ln\frac{kb}{\sqrt{2}} \; .$$

Using Eqs. (3) and (4) we can relate the scattering amplitudes A and B to the differential cross section in the center of mass and the polarization at the c.m. angle θ. By the optical theorem we can relate the total cross section to $A(\theta)$ through

$$\sigma_t = \frac{4\pi}{k} \, \mathrm{Im} A(0) \; .$$

The absorption cross section can be written

$$\sigma_a = 2\pi \int_0^R \left(1 - \frac{1}{2} \left\{ \exp\left[2\,\mathrm{Im}(\chi_c + \chi_s)\right] + \exp\left[2\,\mathrm{Im}(\chi_c - \chi_s)\right] \right\} \right) b\, db \, .$$

B. Discussion of Polarization and Inelastic States

Allowing inelastic states complicates the analysis. To illustrate, let us consider a simplified example--the case of scattering protons by carbon and using an analyzer that cannot distinguish less than 5-MeV loss. We cannot distinguish elastic scatterings from those in which carbon is excited to the first excited state, 4.4 MeV. The polarization of the beam after one scattering would then be an average of the elastic polarization and the first inelastic-state polarization weighted by the probability for producing the states involved:

$$P' = \frac{I_{el} P_{el} + I_{in} P_{in}}{I_{el} + I_{in}} .$$

From a double scattering by carbon, our analyzer would be able to discriminate against those protons which lost 4.4 MeV at each of the two targets, so the asymmetry would be

$$e = \frac{\left(I_{el} P_{el} + I_{in} P_{in}\right)\left(I_{el} A_{el} + I_{in} A_{in}\right) - I_{in}^2 P_{in} A_{in}}{\left(I_{el} + I_{in}\right)\left(I_{el} + I_{in}\right) - I_{in}^2} .$$

The analyzing power for the elastic scattering is identically equal to the polarizing power from time-reversal invariance. Previous experiments have shown that this equality holds for inelastic scatterings also, although this has not been generally shown.[4] Using these equalities we obtain

$$e = \frac{I_{el}^2 P_{el}^2 + 2I_{el} I_{in} P_{el} P_{in}}{I_{el}^2 + 2I_{el} I_{in}} \simeq P'^2 \left[1 + \left(\frac{I_{in}}{I_{el}}\right)^2 \cdot \left(\frac{P_{el}^2 - P_{in}^2}{P_{el}^2}\right)\right] .$$

Note that this is not equal to the square of the average polarization. The difference is small as long as the amount of contamination is small or the polarization of the contaminating state is near that of the elastic.

Polarization induced by inelastic scatters is a complex question. The review article by Squires contains a summary of the experimental data obtained at low energies and a theoretical explanation.[4]

When the proton recoils coherently from a nucleus, even though exciting it, the polarization remains quite similar to that of the elastic scattering. Fortunately, this is the case for a great many low-lying excited states. The 4.4, 9.6, and 12.2-MeV excited states of carbon yield results quite similar to the elastic scattering at 100- to 200-MeV lab energy for the initial protons, and similar results are expected for the higher energies. Other states, such as the 15.5-MeV and 22-MeV almost-elastic states yield almost no polarization.

C. Angular Alignment and Asymmetry Error

Errors in the measured asymmetry are caused by incorrectly matching the first and second angles of scattering for both left-left and right-left scatterings. This appendix relates misalignments in these angles to errors in the measured asymmetry. Since the polarization is a slowly varying function of angle compared to the differential cross section, for this simplified treatment the polarization induced at the first and second targets is treated as a constant, and only errors due to changes in the differential cross sections with variations in angle are considered. Target-out considerations are also ignored.

For practical purposes we may write Eq. (7) for the asymmetry as

$$\epsilon = \frac{I_{LL} - I_{RL}}{I_{LL} + I_{RL}} .$$

Differentiating we find that the error is

$$\Delta\epsilon = \frac{2I_{LL}I_{RL}}{\left(I_{LL} + I_{RL}\right)^2} \left[\left(\frac{d\ln I_{LL}}{d\theta_1} - \frac{d\ln I_{RL}}{d\theta_1} \right) \Delta\theta_1 \right.$$

$$\left. + \left(\frac{d\ln I_{LL}}{d\theta_2} - \frac{d\ln I_{RL}}{d\theta_2} \right) \Delta\theta_2 \right] .$$

On the assumption that the errors are uncorrelated and using the average intensity I defined as

$$I = \frac{I_{LL} + I_{LR}}{2} ,$$

we may write

$$\Delta\epsilon \cong \left(\frac{1}{2}\right)^{1/2} \left(\left| \frac{d\ln I}{d\theta_1} \right| \Delta\theta_1 + \left| \frac{d\ln I}{d\theta_2} \right| \Delta\theta_2 \right) .$$

The intensity is measured by taking the ratio of C, the flux of particles in the counters, to T, the normalized current in the ion chamber at the second target. Using this ratio in the above equation, we have

$$\Delta\epsilon = \left(\frac{1}{2}\right)^{1/2}\left[\left|\frac{d \ln (C/T)}{d\theta_1}\right|\Delta\theta_1 + \left|\frac{d \ln (C/T)}{d\theta_2}\right|\Delta\theta_2\right].$$

These quantities may be empirically evaluated. We can proceed further, however, by remembering that counters see only the elastically scattered particles while the second-target ion chamber reflects particles elastically and inelastically scattered by the first target. Thus we may write

$$\left|\frac{d \ln(C/T)}{d\theta_1}\right| = \left|\frac{d \ln [I_{el}/(I_{el} + I_{in})]t_1}{d\theta_1}\right| = \left|\frac{d \ln(1 + I_{in}/I_{el})t_1}{d\theta_1}\right| \leqslant \left|\frac{d(I_{in}/I_{el})t_1}{d\theta_1}\right|,$$

where this ratio of inelastics to elastics is that produced at the first target. With variations in the second angle of scattering, only the flux of particles arriving at the counters changes, and we may write

$$\left|\frac{d \ln(C/T)}{d\theta_2}\right| = \left|\frac{d \ln C}{d\theta_2}\right| = \left|\frac{d \ln(I_{el})t_2}{d\theta_2}\right|,$$

where this elastic differential cross section is now that of the second target. Combining the previous three equations, we may write

$$\Delta\epsilon = \left(\frac{1}{2}\right)^{1/2}\left[\left|\frac{d(I_{in}/I_{el})t_1}{d\theta_1}\right|\Delta\theta_1 + \left|\frac{d \ln(I_{el})t_2}{d\theta_2}\right|\Delta\theta_2\right].$$

At 730 MeV, the change in the inelastic-to-elastic differential cross section is much less rapid with angle than the percentage change in the elastic cross section, and the results are much more sensitive to the second angle of scattering than the first.

By varying the sense of the first angle and keeping the second angle fixed, freedom is gained from false asymmetries and non-uniformities in the original beam. Let us consider a correlation of the energy distribution of the beam with the position of the beam as it hits the target. Schematically, the beam layout can be represented by the following diagram.
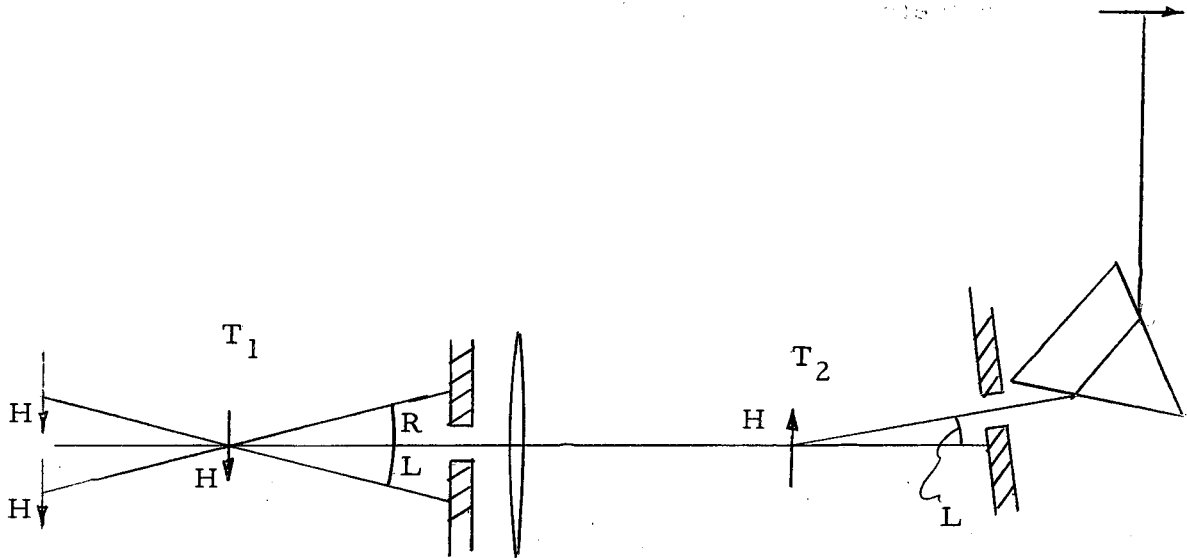
Let us assume that the right side of the beam has a higher energy than the left side. Then this high-energy side is on the right side of the target for both right and left scatters at the first target. Because of the focusing properties of the quadrupole triplet, the image is reversed and the high energy side of the beam is on the left side at the second target. For both right-left and left-left scatterings as the beam prepares to enter the spectrometer, the spectrometer sees the distribution from the same side, and so effects caused by this nonuniformity cancel from the asymmetry. Similarly, irregularities in the beam shape and angular distribution are not reflected in the asymmetry.

However, one effect does not cancel. If, at the first target there is an energy loss that assumes a different distribution across the target for both right-left and left-left scatterings, then this will be reflected in the final particle distribution after the spectrometer. Such a distribution naturally occurs, since the kinetic energy lost in scattering increases with angle. Particles scattering from the right side of the beam at the first target in the right-left geometry have a higher

energy than those from the left side. The reverse is true for left-left geometry. Schematically we have
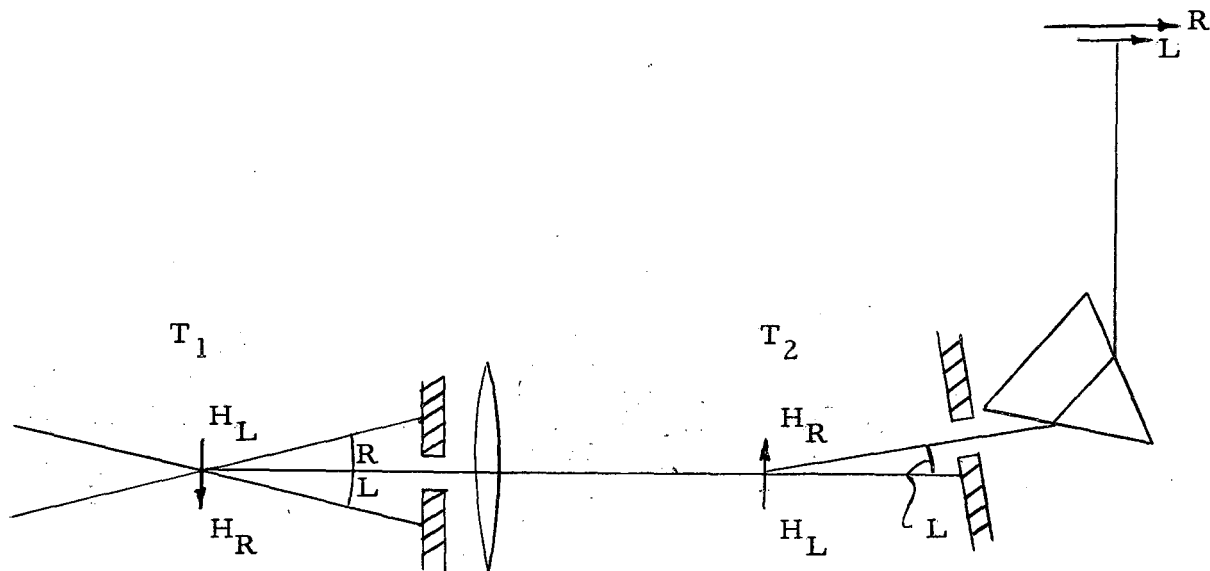
This energy distribution at the second target couples with the disper-sion and focusing of the spectrometer differently for the right-left and left-left scattering. The result is that the final beam distribution after the spectrometer is compressed for left-left scattering and is elongated for right-left scatterings.

Since for nucleon-nucleus scattering the amount of energy lost in small-angle scattering is a very slowly varying function of angle, this effect is of no concern and was not detectable. For nucleon-nucleon scattering, this energy loss with angle amounts to many MeV per degree, and the effect was quite apparent. But for nucleon-nucleon scattering, we know there are no almost-elastic scatterings, and we can integrate over the entire elastic distribution. For this experiment, this means taking the results of the large counter for polarization measurements. Had the spectrometer bent upwards instead of bending in the same plane as the first and second scattering, this problem could have been avoided completely.

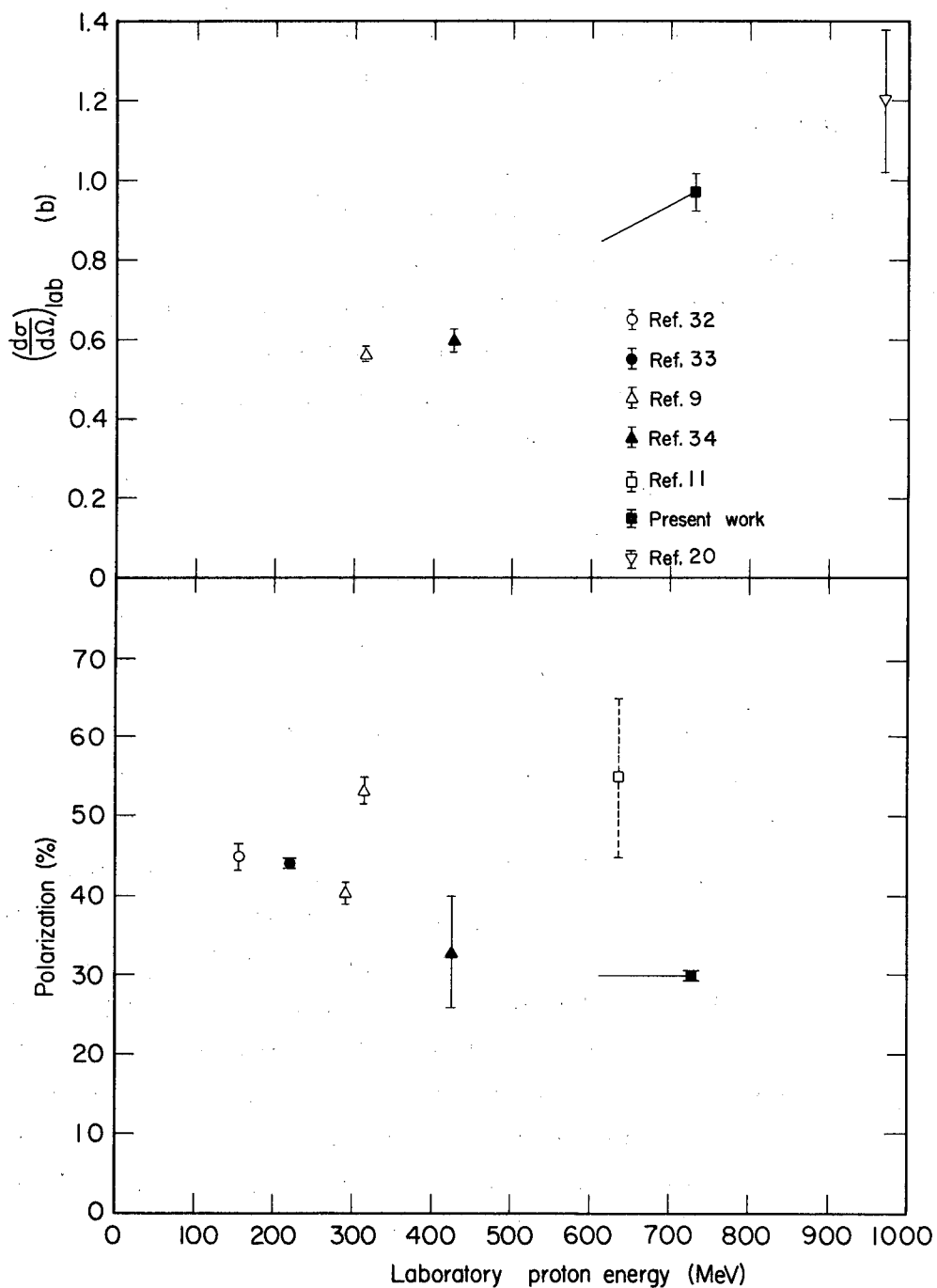### D. Proton-Carbon Data at 6 Deg as a Function of Energy

The differential cross section and polarization of proton-carbon scatterings as a function of energy are needed to analyze the proton-proton scattering. A summary of some results vs energy are plotted in Fig. 14. Polarization at 635 MeV was measured on beryllium. For comparison of these data with those of carbon, the angle was scaled down by the ratio of $9^{1/3}/12^{1/3}$, i.e., radius Be/radius C. The values used are given by the lines drawn on the figure.

Since the energy loss in the laboratory system in scattering through an angle is approximately proportional to the square of that angle, we may relate the energy of the proton-carbon scattering of interest for a particular proton-proton angle of scattering in the laboratory system, θ, by the empirical formula

$$E_{PC} \simeq 730 \text{ MeV} - \frac{118 \text{ MeV}}{(20.5 \text{ deg})^2} (\theta_{deg})^2.$$

The differential cross section at this angle appears to be smoothly varying, and there seems to have been no significant error introduced by assuming its dependence with energy to be that of the line in Fig. 14. The variation of the polarization with energy is much less clear. No simple dependence seems to satisfy all the data. As mentioned earlier, there seems to be reason to suggest that the reported values for 635-MeV proton-beryllium are too large. The most prudent choice at this time seems to be to assume that the proton-carbon polarization does not vary in the energy interval that we need. The reader should be aware of the uncertainty in the proton-proton polarization due to the present lack of data. Refinements to the proton-proton data can be made by using the following formula:

$$P_{corrected} = \frac{P_{reported}}{P_{PC}(E_{PC})/0.3} .$$

Fig. 14. Differential cross section and polarization vs energy
from protons on carbon at 6-deg lab. The dashed point is
from protons scattered from beryllium.

MUB-1731

More information concerning the proton-carbon polarization as a function of energy will be available within a few months. Data obtained by placing a spark chamber after the final counters at the rear of this experimental system will yield this information.

After the end of the experiment, it was realized that the necessary information on the proton-carbon scatterings as a function of energy for calibration purposes could have been simply obtained by employing the same experimental setup as used throughout the run. After carbon was calibrated at full energy with thin targets, the second target could have been replaced with a very thick piece of carbon capable of degrading the beam to a lower energy E'. By measuring the asymmetry, one could calibrate the polarization of this thick target. Then with the targets reversed and the beam degraded at the first target, measurement of the asymmetry yields the polarization at the lower energy E'.

REFERENCES

1. M. H. MacGregor, M. J. Moravcsik, and H. P. Stapp, Ann. Rev. Nuclear Sci. 10, 291 (1960).

2. H. Feshbach, Ann. Rev. Nuclear Sci. 8, 49(1958).

3. L. Wolfenstein, Ann. Rev. Nuclear Sci. 6, 43 (1956).

4. E. J. Squires, Progr. Nucl. Phys. 8, 47 (1960).

5. R. E. Richardson, W. P. Ball, C. E. Leith, and B. J. Moyer, Phys. Rev. 86, 29 (1952).

6. K. M. Gatha and R. J. Riddell, Jr. , Phys. Rev. 86, 1035 (1952).

7. S. Fernbach, R. Serber, and T. B. Taylor, Phys. Rev. 85, 1352 (1949).

8. C. L. Oxley, W. F. Cartwright, and J. Rouvina, Phys. Rev. 93, 806 (1954).

9. O. Chamberlain, E. Segrè, R. D. Tripp, C. Wiegand, and T. Ypsilantis, Phys. Rev. 102, 1659 (1956).

10. M. G. Mescheriakov, S. B. Nurushev, and G. D. Stoletov, J. Exptl. Theoret. Phys. (U.S.S.R.) 33, 37 (1957); Soviet Phys. JETP 6, 28 (1958).

11. M. G. Mescheriakov, S. B. Nurushev, and G. D. Stoletov, J. Exptl. Theoret. Phys. (U.S.S.R.) 31, 361 (1956); Soviet Phys. JETP 4, 337 (1957).

12. Yu. P. Kumekin, M. G. Mescheryakov, S. B. Nurushev, and G. D. Stoletov, J. Exptl. Theoret. Phys. (U.S.S.R.) 38, 1451 (1960); Soviet Phys. JETP 11, 1049 (1960).

13. E. Fermi, Nuovo Cimento Supp. , 10, 17 (1955).

14. William H. McMaster, Rev. Modern Phys. 33, 8 (1961).

15. L. Wolfenstein, Phys. Rev. 96, 1654 (1954).

16. L. Wolfenstein and J. Ashkin, Phys. Rev. 85, 947 (1952).

17. A. Scotti and D. Y. Wong, Phys. Rev. Letters 10, 142 (1963).

18. K. Watson, Revs. Mod. Phys. 30, 565 (1958).

19. W. Riesenfeld and K. Watson, Phys. Rev. 102, 1157 (1956).

20. C. J. Batty, The Scattering of High Energy Nucleons by Complex Nuclei, Rutherford High Energy Laboratory Report NIRNS/R/1, June 1960.

21. R. Hofstadter, Ann. Rev. Nucl. Sci. 7, 231 (1957). R. Herman and R. Hofstadter, High-Energy Electron Scattering Tables (Stanford University Press, Stanford, 1960).

22. T. J. Devlin, OPTIK: An IBM 709 Computer Program for the Optics of High-Energy Particle Beams, Lawrence Radiation Laboratory Report, UCRL-9727, Sept. 1961.

23. D. B. Newhart, V. Perez-Mendez, and W. H. Pope, Liquid-Hydrogen Target, Lawrence Radiation Laboratory Report UCRL-8857, August 1959.

24. L. S. Azhgirei, I. K. Vzorov, V. P. Zrelov, M. G. Meshcheryakov, B. S. Neganov, R. M. Ryndin, and A. F. Shabudin; J. Exptl. Theoret. Phys. (U. S. S. R.) 36, 1631 (1959); Soviet Phys. JETP 6, 1163 (1959).

25. O. Chamberlain, E. Segrè, and C. Wiegand, Phys. Rev. 83, 923 (1951).

26. Lawrence Radiation Laboratory Counting Handbook, Lawrence Radiation Laboratory Report, UCRL-3307 Rev. , January 1959.

27. L. Wolfenstein, Phys. Rev. 75, 1664 (1949).

28. V. I. Maskaliv and B. V. Bavrilovskii, Doklady Akad. Nauk. S. S. S. R. 110, 972 (1956).

29. N. E. Booth, G. W. Hutchinson, and B. Ledley, Proc. Phys. Soc. (London) 71, 293 (1958).

30. V. P. Dzhelepov, V. I. Satarov, and B. M. Golovin, Soviet Phys. JETP 2, 349 (1956).

31. N. R. Mott and H. S. W. Massey, The Theory of Atomic Collisions, second edition (Oxford: Clarendon Press, 1949), p. 48.

32. R. Alphonce, A. Johansson, and G. Tibell, Nucl. Phys. 3, 185 (1957).

33. E. M. Hafner, Phys. Rev. 111, 297 (1958).

34. E. Heiberg, Phys. Rev. 106, 1271 (1957).